# The Statistical Distributions of Evaporation Duct and the Communication Characteristics Over the South China Sea

**Cheng Yang[1,2], Jian Wang[1,2,*], Feng Feng[1]**

[1] School of Microelectronics, Tianjin University, Tianjin, China.

[2] Qingdao Institute for Ocean Technology, Tianjin University, Qingdao, China.

* Corresponding author: Jian Wang (wangjian16@tju.edu.cn)

**Key Points:**

- The spatial-temporal database of the evaporation duct over the South China Sea is established and the statistical distribution is analyzed.
- The transmission loss and the communication effects of six modulation by using the evaporation duct are analyzed.
- A 300km transmission in the South China Sea can be achieved under typical communication parameters in February.

## Abstract

To fully grasp the evaporation duct characteristics and effectively support the application of radio systems in the South China Sea (SCS), we proposed a statistical method by using the remote sensing data and the numerical model. Specifically, three works have been completed: (1) The spatial-temporal database is established with about 0.2°spatial resolution in the SCS during 2011-2020, and has the characteristics of large scope, high timeliness, long term, and high resolution; (2) The statistical distribution is analyzed that the height of evaporation duct is the highest during 12:00-17:00, a “Golden edge” with a height of 20m appears in the coastal area. (3) It is found that the northern coastal channel with a width of more than 300km was formed from May to July. Based on the above statistical results, the transmission loss was quantitatively analyzed that has the characteristics of “pipe adaptation” to different meteorological conditions. In the end, communication effects of 2FSK, BPSK, QPSK, MSK, 16-QAM, and 64-QAM by using the evaporation duct are analyzed, and a usable result shows that a 300km transmission in the SCS can be achieved under typical communication parameters in February. It is hoped that this paper can be further expanded to potentially providing a basis for support the application of the current radio system in SCS and explore a new effective means of communication.

## Plain Language Summary

The evaporation ducts are natural phenomena occurring at the bottom of the troposphere. And it is well-known that an evaporation duct can be considered a layered dielectric waveguide to support the electromagnetic wave propagations with specific frequencies. To fully grasp the evaporation duct characteristics and effectively support the application of radio systems in the South China Sea (SCS), we proposed a statistical method by using the remote sensing data and the numerical model. Specifically, the spatial-temporal database is established in the SCS, the statistical distribution is analyzed, and it is found that the northern coastal channel with a width of more than 300km was formed from May to July. Based on the above statistical results, the transmission loss was quantitatively analyzed. In the end, the communication effects of six typical modulations are analyzed, and a usable result shows that a 300km transmission in the SCS can be achieved under typical communication parameters in February. It is hoped that this paper can be further expanded to potentially providing a basis for support the application of the current radio system in SCS and explore a new effective means of communication.

## 1. Introduction

The evaporation duct in troposphere environments is nature peculiar atmospheric phenomena. It is a kind of surface duct without a base layer generated by the evaporation of water vapor caused by the sea-air interaction under specific meteorological and hydrological conditions. It almost always exists in the oceans over the world. In addition, the height and intensity of ducts vary greatly with geographical longitude and latitude, season, and time of day (Liu et al., 1996; Cheng et al., 2016).

It is well-known that an evaporation duct can be considered as a layered dielectric waveguide to support the electromagnetic wave propagations far beyond the light-of-sight (LoS) at specific frequencies having less attenuation (Stull, 1988; Battan, 1973). Wireless radiowave signals in ultrashort wave and microwave bands can transmit in the tropospheric atmospheric boundary layer formed by the special refractive atmospheric structure (Woods et al., 2009). The variation of the meteorological environment will lead to the variation of the atmospheric refractive index gradient and the evaporation duct parameters, which may also have a great impact on the transmission of the radio system. The evaporation duct benefits the

electromagnetic wave propagations far beyond the LoS and brings many negative effects. The distribution of radar blind area will move with the change of evaporation ducts, and cross time slot co-frequency interference may also occur in the mobile 4G and 5G communication systems. Therefore, the evaporation duct has been a research hot spot in the past decades (Bean et al., 1966; Choi, 1997; Ulate et al., 2018). Significantly, the spatial and temporal distribution law should be understood to make reasonable use of radio systems in the evaporation duct.

To fully grasp and effectively use the evaporation duct, Bean et al. (1966) put forward the relation between atmospheric refraction index and temperature, pressure, and water vapor pressure. They revealed the main synoptic conditions for its formation. Researches on the prediction were gradually carried out based on sea-air interaction theory (Jiang et al., 2020; Ulate et al., 2018). Aiming at SCS, Lin et al. (2005) made a statistical study on the sea area of 100°E ~ 140°E and 0°N ~ 40°N using ocean and ship data from 1982 to 1999. Zhao X. F. et al. (2013) use atmospheric ducts observation experiments data in 2010-2012 spring to make statistics of evaporation ducts, surface ducts, and elevated ducts over the SCS and the tropical eastern Indian Ocean. Estimating the atmospheric duct structure is also possible by using Radar Sea Clutter (Zhao et al., 2012). Cheng Y. et al. (2016) analyzed characteristics of lower atmospheric ducts over the SCS based on Global Position System radiosonde data from 2006 to 2012. Whereas, few types of researches on the grid statistics of evaporation ducts were reported. In addition, more concern for the future is the influence of the environment on the radio system. This influence can be analyzed, and the efficiency evaluation can be realized by combining the meteorological parameters with the theory and method of electromagnetism (Choi, 1997; Booker et al., 1946; Ko et al., 1983). It has important implications for communication system design and provides auxiliary decision information for normal system operating (Wang et al., 2021). This is one crucial starting point of this paper.

The South China Sea (SCS) locates in the south of the Chinese mainland, with a vast natural sea area and rich resources (Yang et al., 2017). Along with the continuous exploration, development, and utilization of the ocean, the activities on the ocean are more and more frequent. The increasing communication demands of marine businesses cannot be met by traditional means. Therefore, a novel statistical method of the evaporation duct is proposed based on meteorological parameters in the latest global assimilation database and the numerical model. A high-resolution spatial-temporal database of evaporation ducts was constructed in the SCS, and the impact of meteorological factors was analyzed. And then, the propagation characteristics are analyzed quantitatively, with typical meteorological parameters in the SCS. In the end, the communication effect will also be analyzed in a specific location and period in the SCS. The investigation in this paper has important implications for evaporation duct communication system design and provides auxiliary decision information for typical systems operating in the SCS.

## 2. Statistical method of evaporation duct

### 2.1 Characteristic of evaporation duct

The density of the tropospheric atmosphere varies both horizontal and vertical, and it has a highly uneven spatial distribution. The direction of an electromagnetic signal will change while propagates in this layer, that is, bending. The bending is related to the atmospheric density, which is usually described by the atmospheric modified refractive index $N$ or the atmospheric modified refractive index $M$. Atmospheric refractive index $N$ is a function of pressure, temperature and humidity in the ideal gas law (Bean et al., 1966). The modified refraction index gradient and the refractive index gradient conform to

$dM/dh = dN/dh + 0.157$ in the microwave frequency band, where $h$ is the height above the earth. The bending degree of the electromagnetic wave is mainly affected by the vertical change of the refractive index gradient. The propagation curvature of the electromagnetic wave bending to the ground is greater than of the earth when $dN/dh < -0.157$ (i.e. $dM/dh < 0$), which is called super-refraction. The atmosphere is trapped in a refraction condition at this time, and the trapped layer is called atmosphere duct.

Atmospheric ducts can be divided into surface ducts and elevated ducts within different heights; the evaporation duct is a baseless surface duct. The evaporation duct is mainly generated by the evaporation of the sea due to the interaction between sea and air under specific meteorological conditions. The vertical humidity gradient varies with the change of altitude. It is the structure of the lower atmosphere which often appears in the atmospheric boundary layer of the ocean. It generally exists above the ocean surface and has a high utilization rate, which can play an important role in supporting the long-distance and large-bandwidth transmission of high-frequency signals in the SCS.

## 2.2 Statistical method of evaporation duct

### 2.2.1 NCEP Meteorological Datasets

The generation of the duct is closely related to meteorological and hydrological conditions at different scales. To judge the existence of the atmospheric duct, it is necessary to measure the structure of the atmosphere and diagnose it according to the characteristic of the modified refractive index. Direct measurements (Liu et al., 1979; Hao et al., 2016), inversion methods (Yardim et al., 2007; Yardim et al., 2012) and numerical models (Paulus et al., 1985; Musson-Genon et al., 1992; Babin et al., 1997; Frederickson et al., 2000; Fairall et al., 2003; Grachev et al., 1997; Newton, 2003) are main measurement methods.

Direct measurements mainly use microwave refractive index meter, meteorological gradient meter, or low altitude atmospheric sounding system to measure the atmospheric characteristics at various heights. The defect can only achieve single or multi-point detection and cannot acquire meteorological element data in a large area. Unlike direct measurements, numerical methods obtain the characteristics of the duct by converting the meteorological parameters at the specified height (Zhao et al., 2021; Zhu et al., 2018). Wide area, high resolution, long-term, near real-time, and low-cost analysis can be realized by introducing remote sensing data. At present, public data sources required for the analysis of the evaporation duct characteristics mainly include such as National Centers for Environmental Prediction (NCEP) Climate Forecast System (CFS) Selected Hourly Time-Series Products (Saha et al., 2012), European Centre for Medium-Range Weather Forecasts (ECWMF) Datasets (Zuo et al., 2019), National Snow and Ice Data Center (NSIDC) Datasets (Mcallister et al., 2014), National Data Buoy Center (NDBC) Datasets (Surhone et al., 2011), etc.

In this paper, meteorological parameters data from the second version of the NCEP Climate Forecast System Version 2 (CFSv2) were selected as dataset source input. The NCEP and National Center for Atmospheric Research (NCAR) are cooperating in the recovery of observation data from land, surface, ships, radiosonde, aircraft, and satellites (Saha et al., 2012); NCEP CFSv2 was made operational in March 2011. The products here are available at 1760 x 880 grid points hourly, and its supplied data is with 0.205°-0.204° from 0° E to 359.795° E, and 89.843° N to 89.843° S. These datasets are usually updated at the beginning of the month, as the longest analysis data in the time series of climate analysis, it has been widely used in climate diagnosis and analysis. While analyzing the characteristics of the evaporation duct, five meteorological parameters need to be taken into account: the

pressure and temperature at the surface, the relative humidity (RH) and temperature at the height of 2m above the ground and sea surface, and the wind speed data at the height of 10m above the surface (Yang et al.,2009).

### 2.2.2 NPS Model

The numerical methods of evaporation ducts are generally based on the Monin-Obukhov similarity theory (Fairall et al., 2003; Grachev et al., 1997). That is, the variation of atmospheric refractive index with altitude near the sea can be obtained by the observation data of hydrometeorological parameters. Then the evaporation duct height (EDH) will be determined. We can analyze the atmospheric refractive index profile through the Paulus Jeske (PJ) model (Paulus et al., 1985), the Musson Gauthier Bruth (MGB) model (Musson-Genon et al., 1992), the Babin Young Carton (BYC) model (Babin et al., 1997), and the Naval Postgraduate School (NPS) model (Frederickson et al., 2000) to obtain the height and strength of evaluation duct.

NPS model has been verified in previous studies (Babin et al., 1997; Shi et al., 2019; Babin et al., 2002; Grachev et al., 2007), and match best with the measured data (Frederickson et al., 2000). It obtains the profile of temperature, humidity and pressure first. And then, the profile of the atmospheric refractive index is calculated with the relationship between the atmospheric refractive index and temperature, humidity, and atmospheric pressure. The vertical profile of temperature T and specific humidity Q in the surface layer is calculated as (Burk et al., 2003):

$$T(z) = T_0 + \frac{\theta_*}{\kappa}\left[\ln\left(\frac{z}{z_{0t}}\right) - \psi_h\left(\frac{z}{L}\right)\right] - \Gamma_d z \tag{1}$$

$$q(z) = q_0 + \frac{q_*}{\kappa}\left[\ln\left(\frac{z}{z_{0t}}\right) - \psi_h\left(\frac{z}{L}\right)\right] \tag{2}$$

where $T(z)$ and $q(z)$ are the air temperature and specific humidity at altitude *z* respectively; $T_0$ and $q_0$ are temperature and specific humidity at sea surface respectively, with $q_0 = 0.98 q_s(T_0)$ , $q_s(T_0)$ is the saturated specific humidity of sea surface calculated based on sea surface temperature (Alappattu et al., 2016); $\theta_*$ and $q_*$ are the characteristic scales of potential temperature $\theta$ and specific humidity $q$ respectively; $\kappa$ is Karman constant; $z_{0t}$ is thermodynamically roughness height; $\psi_h$ is temperature universal function ; $\Gamma_d$ is the dry adiabatic decline rate, approximately equal to 0.00976K/m; $L$ is the similarity length.

By combining the NCEP reanalysis data and the NPS model, the variation of atmospheric refractive index with height can be obtained. It provides statistical methods for studying the characteristics of evaporation ducts in the SCS.

## 3. Statistical characteristic of evaporation ducts in the SCS

### 3.1 Spatial and Temporal Distribution of EDH

In this paper, the reanalysis data from 2011 to 2020 in the NCEP database were used for statistical analysis. The EDH was calculated by import the meteorological parameters with the NPS model. The spatial and temporal distribution of the EDH over the SCS (105°E ~125°E, 5°N~25°N) in different years and months was statistically analyzed by using the

statistical method. The spatial and temporal distribution characteristics are shown in Figure 1 - Figure 6. The statistical results of the lower quartile, median, and upper quartile in different years, months, and hours were calculated by different colored boxes, respectively. The remaining points were distributed around the box with the sign of "+" to establish the extension line of "whisker". These conclusions can be drawn:

(1) Different regional results for typical characteristics of the evaporation duct with hours are shown in Figure 1, and statistical results are illustrated in Figure 2. The overall of EDH varies slightly with hours periodically, and it stays intense during the afternoon and weak before sunrise. From 6:00 to 8:00, the evaporation of the ocean gradually strengthened with the rising temperature, and the EDH gets increased as a result. It increased gradually during the day and reached the highest at 18:00, with an average height of 11.1m. Then decreases slowly during the night, and the average height reaches the lowest at 5:00 am, reaching 8.98m. Central SCS regions such as Sansha City remained stable throughout the day, only falling before sunrise. In the afternoon, the "Golden edge" appeared in the northern and western coastal areas from 12:00 – 18:00, and EDH was significantly higher than that in the other areas. Hainan Island and its surrounding areas have unique distribution characteristics. The overall EDH in the surrounding sea area is higher than that of the SCS.

(2) From consideration of Figure 3, EDH in the SCS changes significantly with the change of month. From January to March, the EDH is higher in the western and eastern coastal areas, but lower in the northern coasts. It tends to gather towards the northern coast from April to June, but gradually decreases in the eastern and western coasts. The northern coastal channel with a width of more than 300km was formed in June. Most of the EDH exceeded 20m, then decreased to less than 10m in September. The height in the western and eastern coastal areas gradually increases to over 10m in most areas after the winter. In terms of spatial distribution characteristics, a large area with EDH exceeding 15m appeared in Southeast Asia's land area from December to March, which is uncommon in the inland area. However, as the temperature increases, the height decreases to the normal level in the inland area (which is less than 5 m). From March to July, it can be seen that the duct channels form out around Hainan Island. It starts with a slight piece of the Gulf of Tonkin, then increases to cover the western region. Finally, an "evaporation ducts corridor" connecting Hainan Island and Taiwan Island with a height of more than 20m will be formed in June.

(3) Monthly statistical results are basically the same as the chart in Figure 4. EDH is relatively stable in spring and winter, but fluctuates greatly in summer and autumn, showing the form of sinusoidal fluctuation as a whole (Haack et al., 2001). It was significantly lower in May, July, and September, the lowest height in September was 8.919m. The EDH reached the highest in June, which was 10.33m. In winter, the EDH is more condensed and balanced, corresponding to the difference in the whole region is small and stable.

(4) Figure 5 shows the annual regional results of SCS. The overall EDH in inland areas of China is lower than 5m, but the situation is different that EDH in most positions exceeds 10m in Southeast Asia's land area such as Vietnam and Cambodia. The overall distribution in Sansha city is connected into the central SCS, and the EDH is between 10m and 12m which represents the characteristics of the overall height. The greatest annual changes in the SCS are mainly reflected in the coastal areas of Hainan Island, the duct was significantly less active in 2011, and the height is mostly between 11m and 12m. EDH increased significantly in 2015 and 2019, and it exceeds 15m at the typical

position.

(5) The annual statistical result of the SCS in Figure 6 also shows some features of annual statistics. Statistical height was higher in 2015 and 2019, and the mid-value is 10.19m and 10.34m, respectively. Mid-value in 2017 is the smallest in 10 years, which is 9.612m.

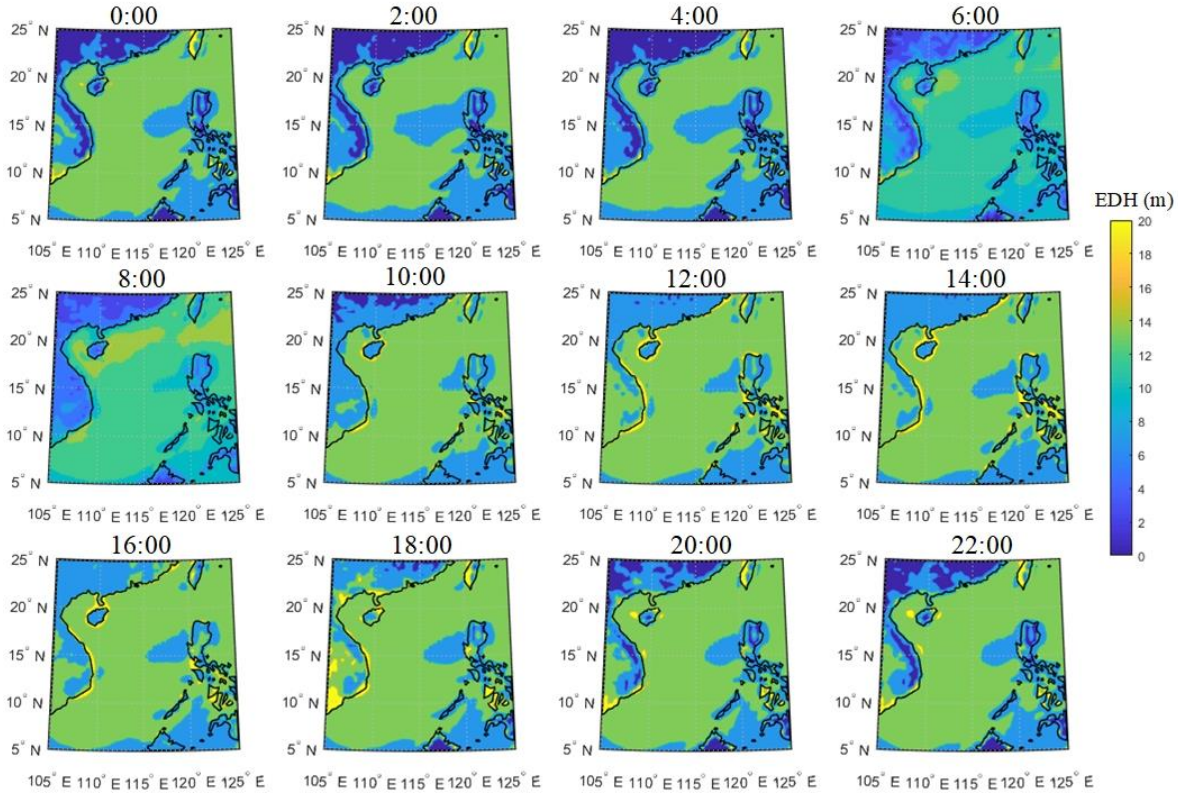


**Figure 1.** Regional EDH statistics in hours.

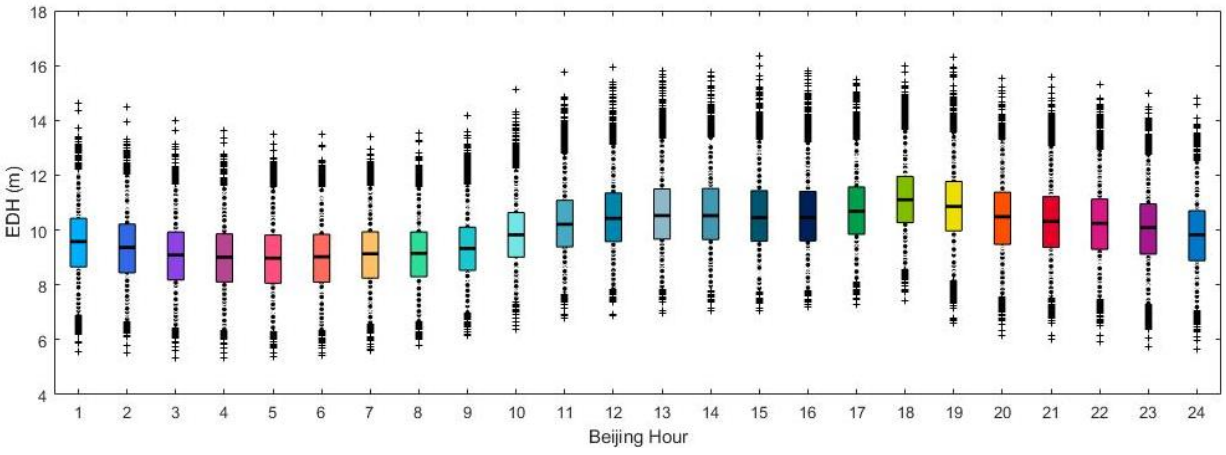


**Figure 2.** Hourly statistics results of EDH in the SCS.

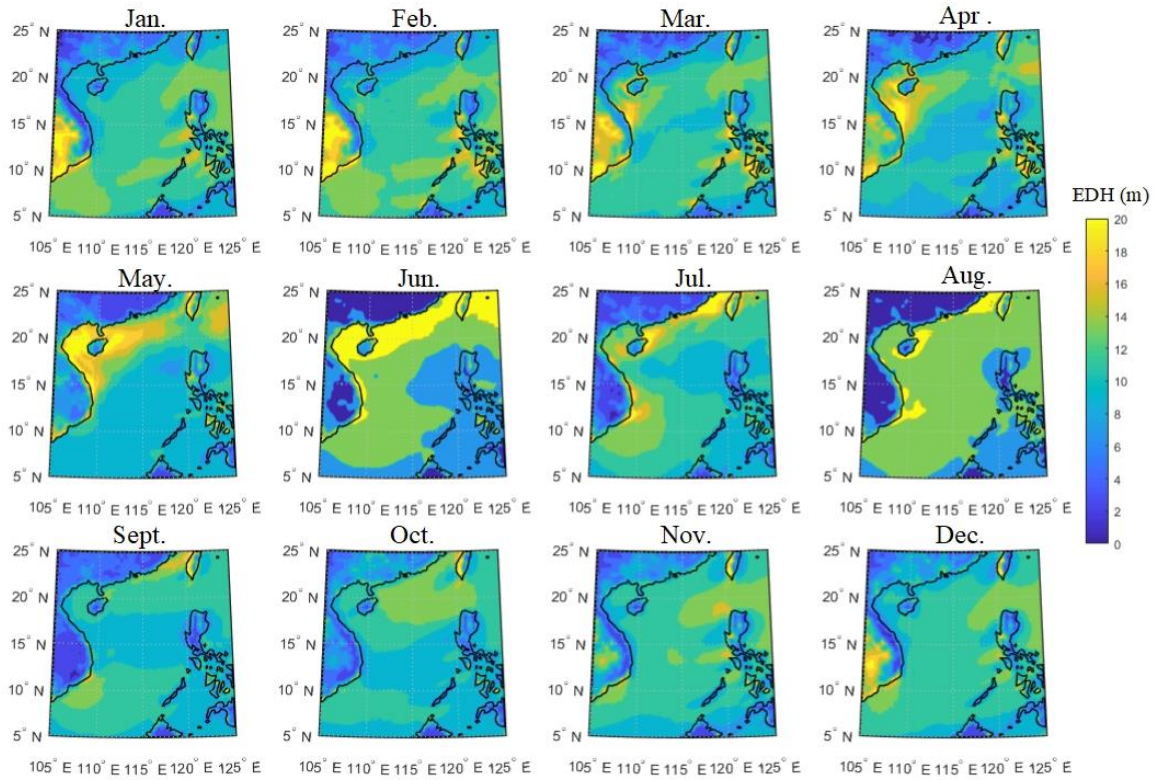


250

251 **Figure 3.** Regional EDH statistics in months.

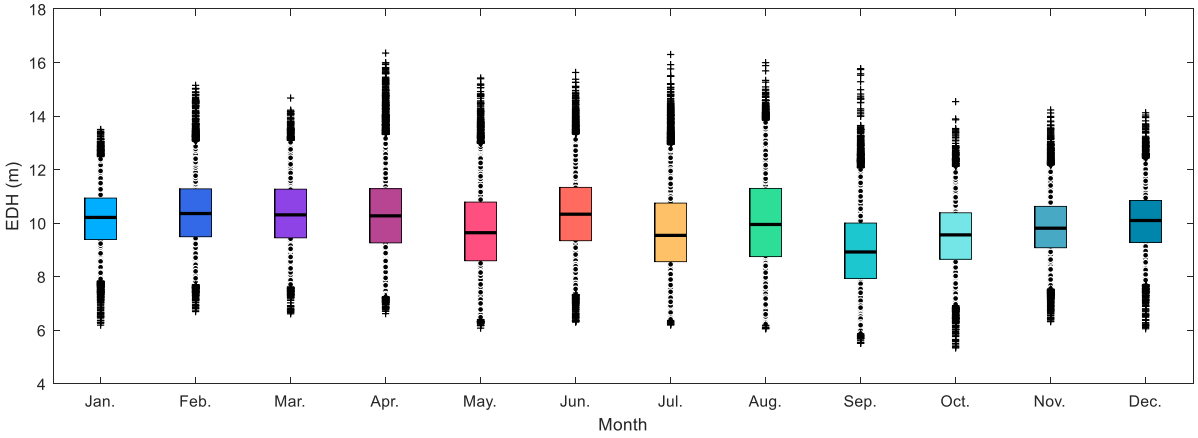


252

253 **Figure 4.** Monthly statistics results of EDH in the SCS.

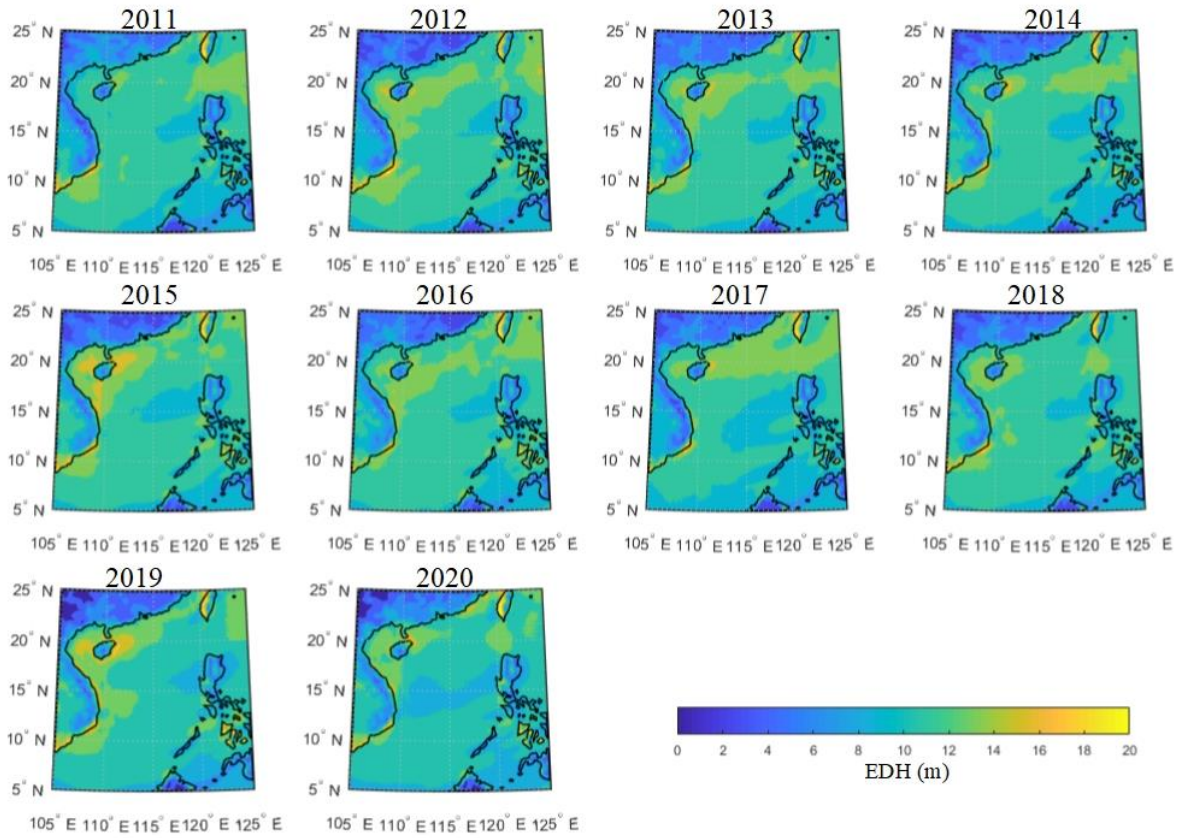


**Figure 5.** Regional EDH statistics in years.

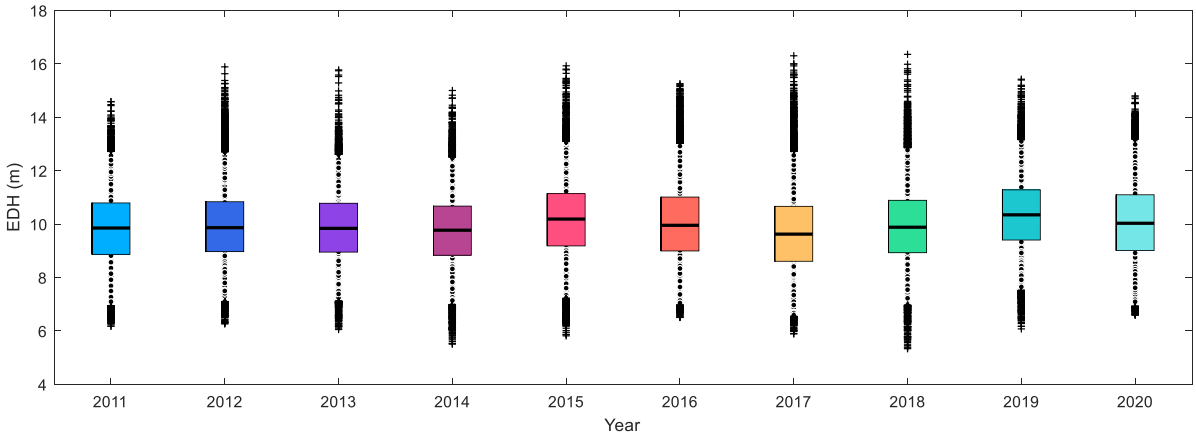


**Figure 6.** Yearly statistics results of EDH in the SCS.

### 3.2 Distribution of EDH in typical positions

According to the statistical results of different years and months, it can be seen that the distribution of EDH in time is not uniform. The SCS is a complex region with a long coastline in the north and west, islands in the east and south, and a deep-sea in the middle, which brings the uncertainty of the change of EDH. NCAR data from 2011 to 2020 was used to conduct statistics on typical positions in the SCS in order to have a deeper understanding of the characteristics of EDH, and the statistical results are shown in Figure 7. The SCS is divided into five typical areas: land-sea interface, inland, coastal land, island, and Mesoneritic fascia, the region types and EDH are represented by circles of different colors and sizes correspondingly. The Inland region far from the ocean is the lowest and is only 2.475 m,

while the highest EDH reaches 18.38 m around the Taiwan Strait in the Land-Sea interface area. It shows the most stable in the Mesoneritic Fascia area, and the overall value of this area remains at a high level.

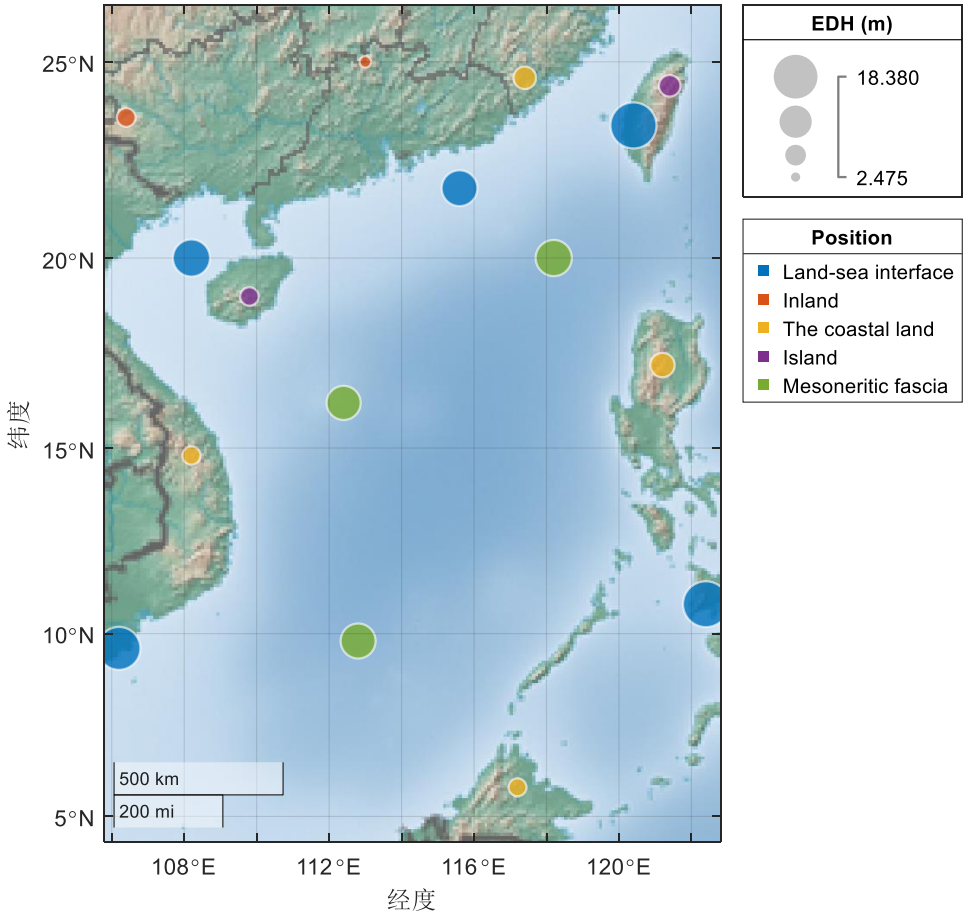


**Figure 7.** The statistical results of EDH at typical locations in the SCS.

Over time, different positions show disparate trends. Figure 8 shows the statistical results of EDH at typical locations using meteorological data over the last 10 years. These conclusions can be drawn:

(1) The Inland and Central SCS fluctuate little with monthly and annual changes. EDH at Inland is lower than 5m all year-round, and the average height is 2.47m. It is relatively high in spring and winter with the maximum value reaches 7.49 m, especially in 2019 and 2020. The height of Central SCS is maintained between 10m - 12m, and the average height is 11.20 m.

(2) Typical location from the "northern coastal channel" was selected to represent for Land-Sea Interface area. The prominent feature is that EDH increase from April to August obviously with the temperature rise. The highest height was 18.95 m in June., and it is more uniform in other months, at about 10m.

(3) Changes in the coastal land region with a month present a unique statistical law, which first decreases and then increases throughout the year. The EDH is at its maximum in spring and winter. EDH reached its maximum at 8.07m in December and reached the lowest at 3.37m in May.

(4) Statistics of Hainan Island reflect the typical distribution of islands in the northern SCS.

The average height is 5.12m, the statistical characteristic is similar to the Land-Sea Interface area but significantly lower. Height in spring and winter is very low, mostly about 3m; it increases greatly in summer and reaches 7.12 m in June.

(5) Taiwan Strait maintains a high average height of 18.37 m all year round, which was the highest EDH in the SCS. Monthly variation conforms to a certain statistical distribution law that it keeps low in spring and winter, increases smoothly in summer and autumn. The highest EDH reaches 21.71m in July.

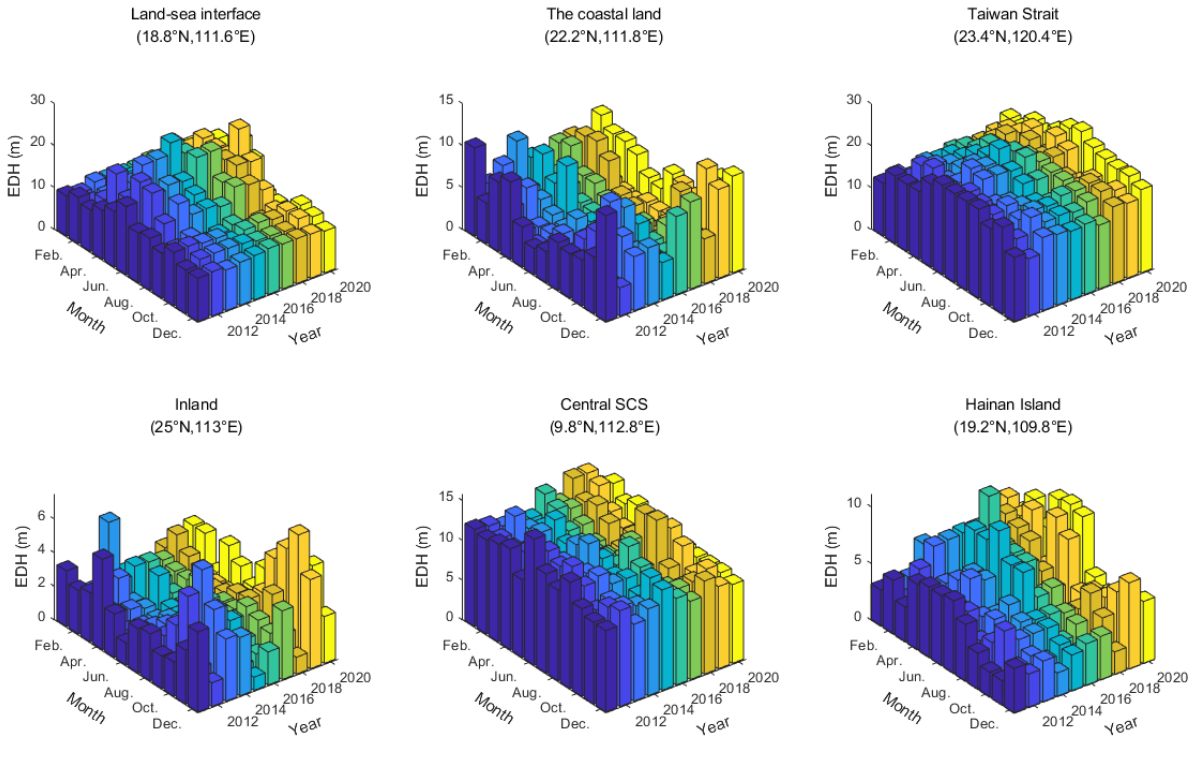


**Figure 8.** Statistics results at typical locations in the SCS.

## 3.3 Analyzation of meteorological factors impacted on evaporation ducts

### 3.3.1 Regional Characteristic Analyzation

The atmospheric duct is determined by the vertical gradient of meteorological parameters, and the EDH is closely related to it (Bean et al., 1966). The strength of evaporation results in the difference in the probability and strength of the duct directly. The ocean current in the SCS is complex, including Kuroshio Current (also known as the warm Japanese current) and Taiwan Current (Feng et al., 2015), which will have a great influence on the characteristics of the evaporation ducts. Spatial and temporal distribution of meteorological parameters including air-sea temperature difference (ASTD), wind speed, and RH was used to analyze the formative factor of evaporation ducts in the SCS. The hourly, monthly, and annual statistical results are shown in Figure 9 - Figure 11 respectively. Conclusions can be obtained combined with the EDH statistics results:

(1) Figure 9 shows a diagram of Regional meteorological parameters statistics in hours. The overall wind speed of the ocean is relatively stable in hourly statistics, while ASTD and RH get a regional change from 8:00 to 16:00. ASTD is above 0 in the inland of China and the coastal areas of West Asian countries at 8:00, and mainly stay in neutral or unstable conditions (ASTD $\leq$0) the rest of the time. The RH increased significantly from 8:00 to 14:00, and it reaches 90% at 12:00 in the Northern coastal area, which creates

favorable conditions for the elevation of the EDH. The air temperature at night is lower than SST, and the ASTD is the smallest at 6:00, which leads to the lowest EDH. Compared with the Central SCS, the meteorological characteristics of Hainan Island are more consistent with the inland area. In the afternoon, the evaporation ducts at the northern and western coastal area maintain in the neutral state, and the wind speed is stable and small (less than 2m/s), which result in a "Golden edge" along the coast in Figure 1.

(2) In Figure 10, the overall meteorological parameters can be divided into two phases. In stage I, from November to March, the southern SCS was in a neutral or stable state (ASTD $\geq$ 0), the wind speed is not high, the RH is about 80%. The northern coastal area was in an unstable state (ASTD < 0), and the wind speed was relatively high (greater than 5 m/s) causes the EDH maintained at a low level. The southern SCS is mainly under neutral and unstable conditions in the second stage from April to October. The RH is about 80%, and the SST is high, which maintains a stable and strong evaporation condition. The increase in wind speed is the main reason for the high EDH in some regions. The state has been neutral or stable since April, and the EDH began to rise while the wind speed decreased significantly in the western area of Hainan island. This trend gradually spread from west to east over time and finally formed a "channel" along the northern coastal area in June. ASTD gradually decreases since July, and the concentrated duct region gradually dissipates, along with wind speed begins to strengthening. In southeast Asia's land areas such as Vietnam and Cambodia, it is in a neutral or stable state throughout the year (ASTD $\geq$ 0), the wind speed is not high, and the RH becomes the decisive factor of EDH. RH from January to March is low, which is good for the EDH to maintain a high level. Since April, the EDH starts to decreases when the RH increases.

(3) According to the statistical chart in Figure 11, the characteristics of each year are not obvious. The difference in meteorological parameters is mainly reflected in 2015 and 2019, the overall wind speed in the western coastal area was significantly lower than that in other years, and the RH was also reduced. Under a neutral or unstable state, this will result in a certain elevation of the EDH. Influenced by its special terrain, the northwest region of the Philippines has the unique characteristics distribution of current and wind speed which separate from the SCS. It also leads to the emergence of the EDH protruding region similar to the "duck bill". The near-sea surface around Hainan Island is mostly in a stable state or neutral state (ASTD $\geq$0) compared with other years in 2015 and 2019. It is coupled with low wind speed and RH in this area, which will form a very high EDH.

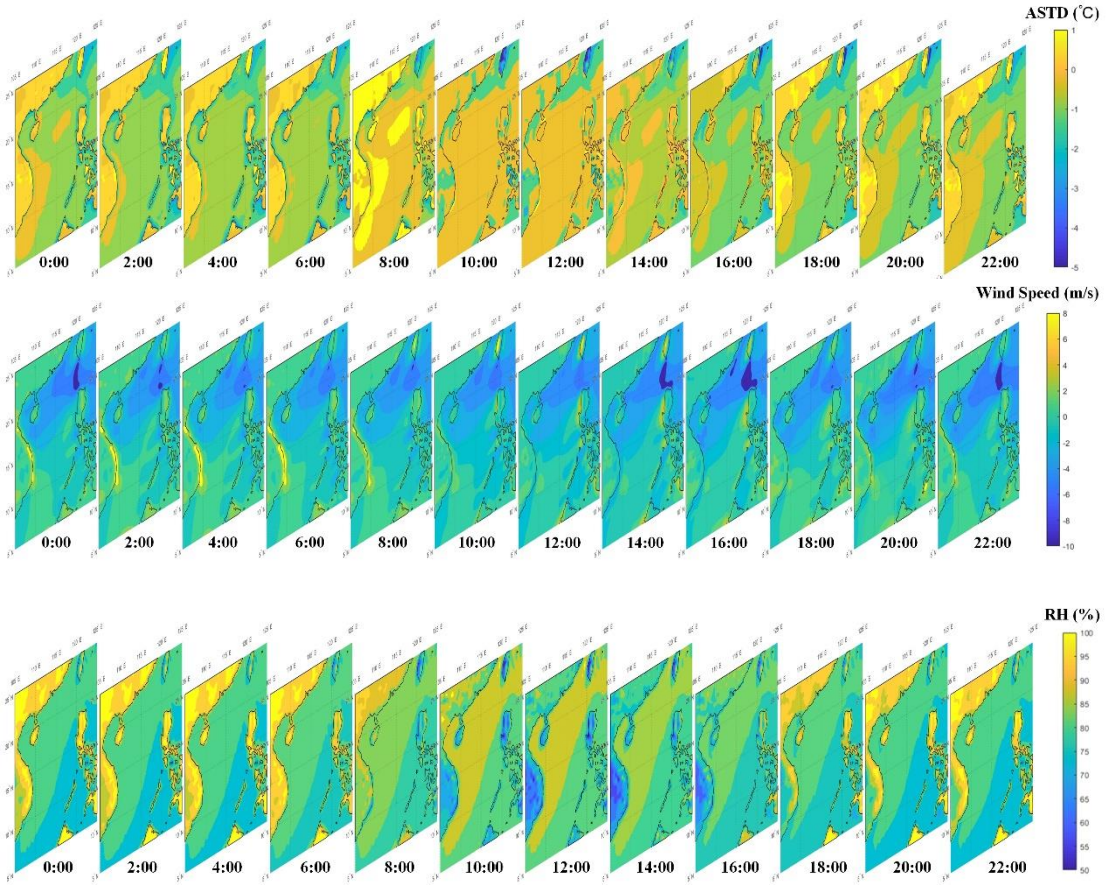


**Figure 9.** Regional meteorological parameters statistics in hours.

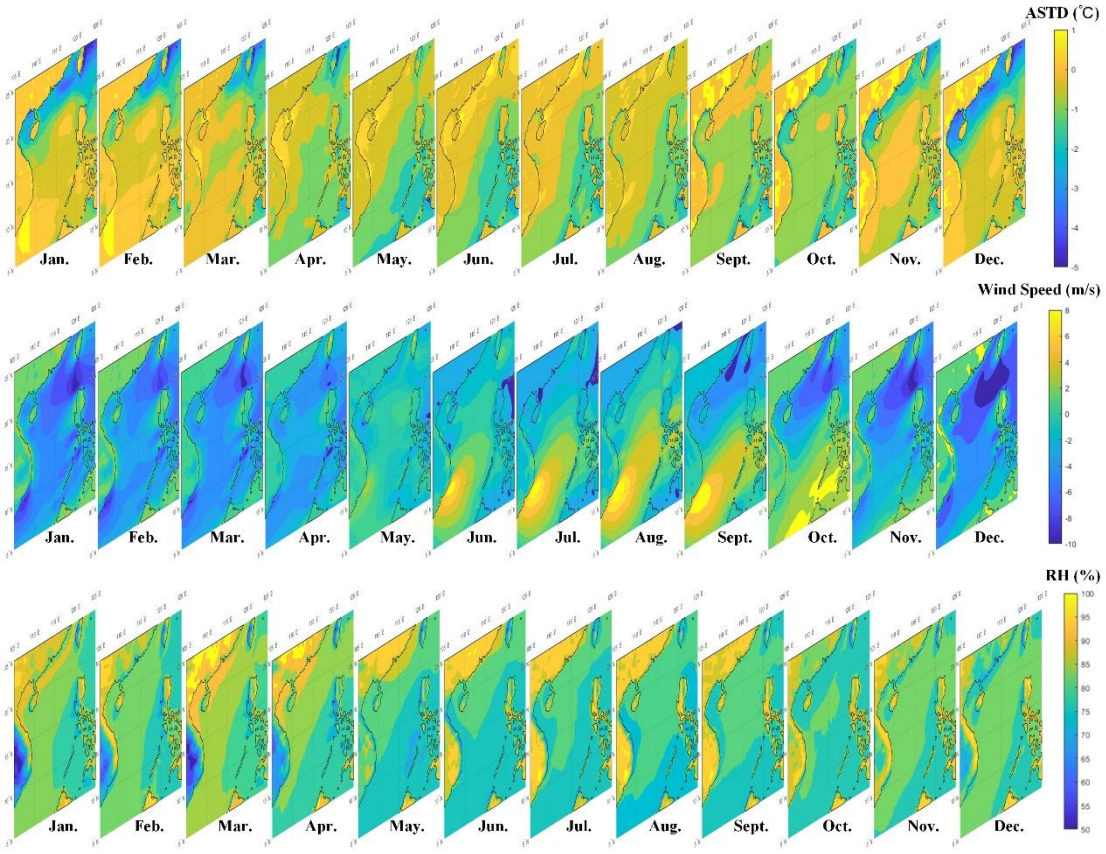


**Figure 10.** Regional meteorological parameters statistics in months.

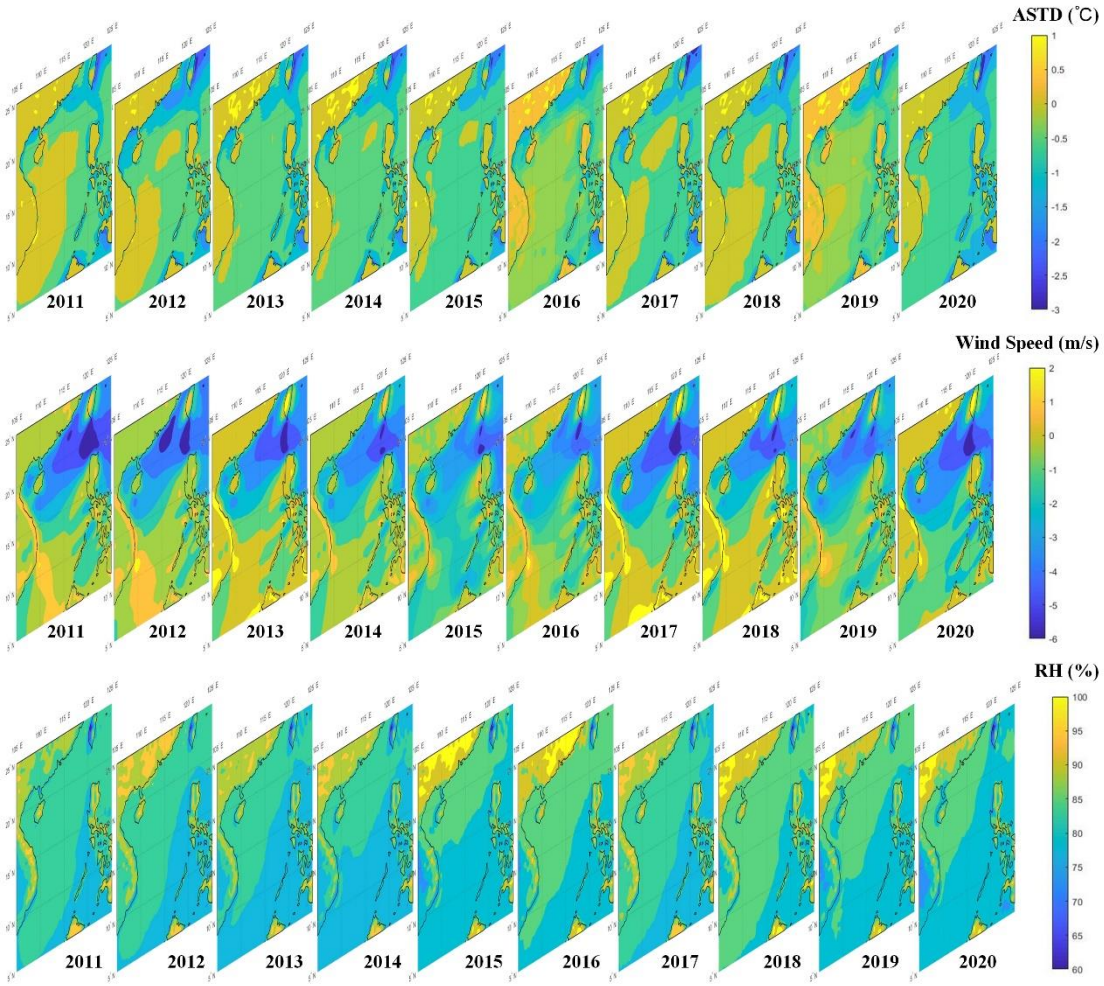


**Figure 11.** Regional meteorological parameters statistics in years.

### 3.3.2 Analyzation in Typical Position

From consideration of formation for the evaporation duct distributions at typical positions, meteorological parameters at typical positions from 2011 to 2020 are collected and displayed in Figure 12. It can be seen that:

(1) The annual statistical results show that the overall meteorological parameters barely change with the year, except the RH varies within a small range. It can be seen that SST in the land-sea interface, Taiwan Strait, and Central SCS area is significantly higher than the other three types of areas, the overall ASTD is less than 0, and the evaporation is maintained at a high intensity. RH in Taiwan Strait is obviously lower, which is the key factor for EDH to maintain the high level. The average wind speed at the Land-Sea Interface was larger than that in other regions, which may lead to the sudden increase of EDH. On the other hand, the variation law of meteorological parameters in the coastal land, Inland, and Hainan Island areas with time are basically consistent, which also reflecting similar duct distribution characteristics.

(2) The statistical rules of day and month in the coastal land, Inland, and Hainan Island areas are similar. The difference between Hainan Island and the other two areas is that its RH distribution is opposite, the RH decreases in summer and autumn, resulting in the rise of the EDH. The condition in coastal land is similar to the Inland, which maintains a neutral state, and the wind speed is stable and small (less than 2m/s). When the RH decreases in

spring and winter, it is easy to cause the elevation of EDH.

(3) The diurnal variation region of the land-sea Interface is also not obvious. In terms of monthly statistical law, the wind speed is higher in spring and winter, and the RH is generally less than 80%, which is the key point that the EDH can still maintain about 10m in winter. With the unstable state in January gradually transitions to a neutral or stable state, wind speed decreased significantly, which indicating the lift of EDH.

(4) Meteorological parameters in Taiwan Strait have a stable day and night variation pattern. SST and wind speed are low during the night, and the state of the duct gradually changes from stable to unstable with the sunrise, along with the wind speed and RH gradually increases. After 12 o'clock, the parameters gradually recovered to the initial state. Parameters in this region vary little with the change of month, and ASTD fluctuates around the neutral state. As the northern sea area, the average surface water temperature of June in Taiwan Strait reaches 28.41 ℃ due to the influence of the Kuroshio Current (Feng et al., 2015), and the average SST in January also reaches 19.58 ℃. Strong evaporation in the sea surface occurs throughout the year, which is conducive to the formation of evaporation ducts.

(5) Central SCS is in a neutral or stable station all year-round, and the influence of wind speed is the main factor that causes the variation of height. Meteorological parameters of high SST, low wind speed, and about 80% RH provide excellent conditions for the duct to maintain a long-term high level.

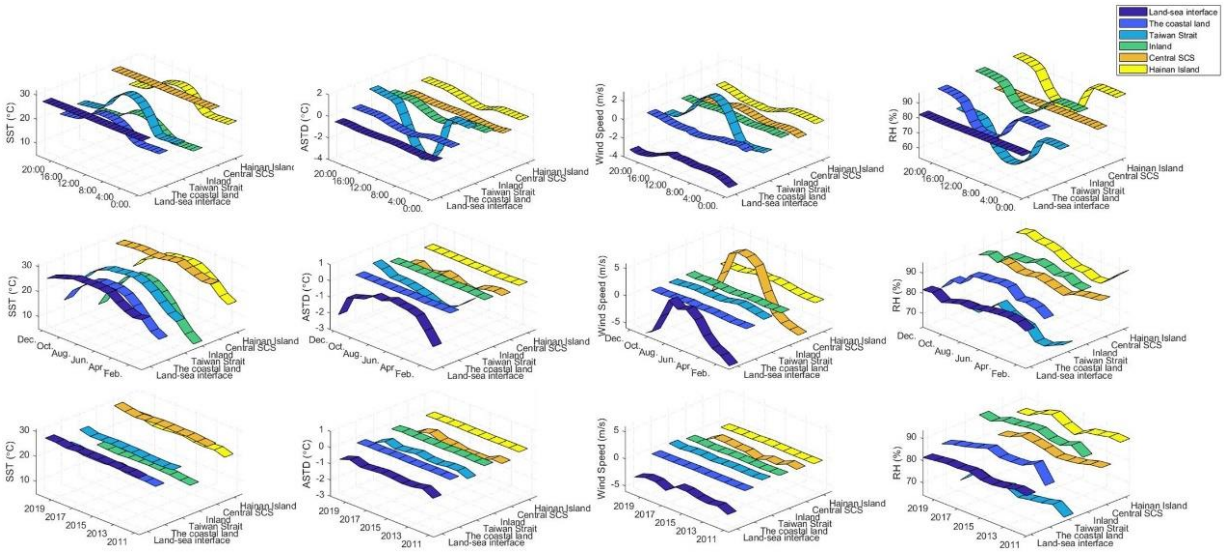


**Figure 12.** Meteorological parameters statistics in typical positions.

## 4. Propagation characteristics of evaporation ducts in the SCS

### 4.1 Impact of meteorological parameters on the propagation characteristics

The spatial and temporal distribution of evaporation ducts in the SCS is analyzed in the last section. The final purpose of the statistics is to master the propagation effect and provide auxiliary decision information for communication. Variations of meteorological parameters may lead to qualitative change of atmospheric refractive index profile, which will affect the regional propagation characteristics, and may also impact the transmission effect in the communication system.

Based on the typical meteorological parameters in the SCS, the effects of meteorological parameters on the propagation were quantitatively analyzed with Advance Propagation Model (APM) with parabolic equation (PE) (Barrios et al., 2002; Barrios et al., 2006). The APM model allows the refractive index to vary with the distance and takes into account the conditions of the surface or sea to consider the influence of the environment on the electromagnetic wave propagation under different conditions as much as possible. The efficient Split-step/Fourier method was adopted to calculate propagation loss step by step in range (Hardin et al., 1973). Transmission on the evaporation duct generally adopts the microwave frequency band above GHz (Gary et al., 1990). Figure 13 shows modified refractivity profiles and transmission loss at 10 GHz in different meteorological conditions. Control variate includes air temperature, sea surface temperature, relative humidity, pressure and wind speed was used to analyze the modified refractivity profiles, transmission loss calculated with 9 m transmitting height and 8m receiving height under different modified refractivity profiles are also given.

These conclusions are drawn from Figure 13:

(1) In Figure 13a), analysis results of refractive index profile and transmission loss with the air temperature varies from 24$^{o}$C to 29 $^{o}$C were revealed, respectively. The process of air temperature from low to high represented the process from unstable to neutral to stable condition, with the EDH increasing sharply and then decreases rapidly. The transmission loss chart presents an optimal "pipe" with ASTD varies from 0 ℃ to 3 ℃, and the minimum loss is about 140dB. The undulating middle part verifies the appearance of the duct, that is, the process of the electromagnetic wave signal reflected and transmitted through the upper and lower layer. EDH decreases rapidly when the air temperature exceeds this range, and the transmission loss at 500 km increased from 150.28 dB at 28 $^{o}$C to 315.41dB at 29 $^{o}$C.

(2) Figure 13b) show the analysis results of the SST varies from 21 $^{o}$C to 26$^{o}$C, which shows the process from stable to neutral to unstable. The change rule is similar to that of air temperature, with the best transmission loss "pipe" appears at 22.4 $^{o}$C ~25 $^{o}$C. The transmission effect shows the best when it is in critical neutral or stable condition, a longer transmission range can be got under the same equipment parameters. The strength of the evaporation is small with the low air temperature, which will affect the signal transmission; large ASTD may also lead to the decrease of EDH, resulting in the increase of transmission loss.

(3) The EDH and strength decrease gradually with the increase of RH in Figure 13. Under neutral conditions, the increase of RH will lead to the gradual decline of EDH when the wind speed is low, and the higher the RH is, the faster the EDH decreases. Transmission loss decreases gradually at first and then increases rapidly, and it gets best when the RH is 70%. Propagation loss is relatively reduced when the height and strength gradually decrease with RH varies from 40% to 70%, mainly because the distance between the upper and lower boundary is far, and the energy diverges more during transmission.

(4) The EDH and strength increase slightly as the wind speed increases, and the transmission loss decreases rapidly in Figure 13. The transmission loss gets lowest when the wind speed is 12m/s. Under the neutral condition, EDH increases gradually at first and then decreases gradually. The initial height is 8.2m when the wind speed is low (2m/s), it rises steeply to 11.3m when the wind speed increases to 4m/s and then remains stable. The maximum EDH is generated 8-10m/s and then decreases slowly with the increase of wind speed. The overall law of transmission loss is basically the same as the height, and more extensive loss occurs when EDH is lower than the antenna height when the wind.

speed is 2m. When wind speed exceeds 4m/s, the fluctuation range of transmission loss is less than 20dB.

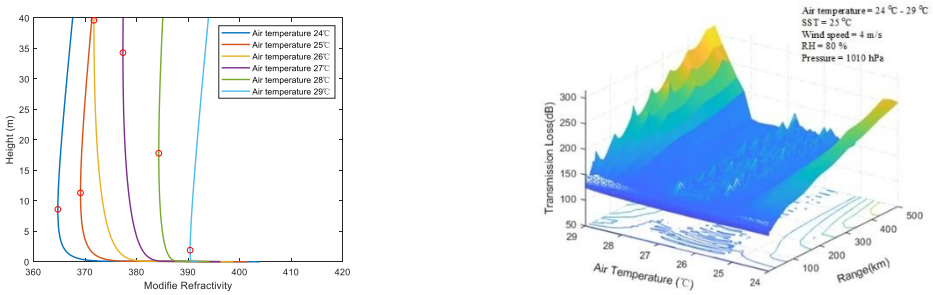


**a)** Transmission loss under different air temperature

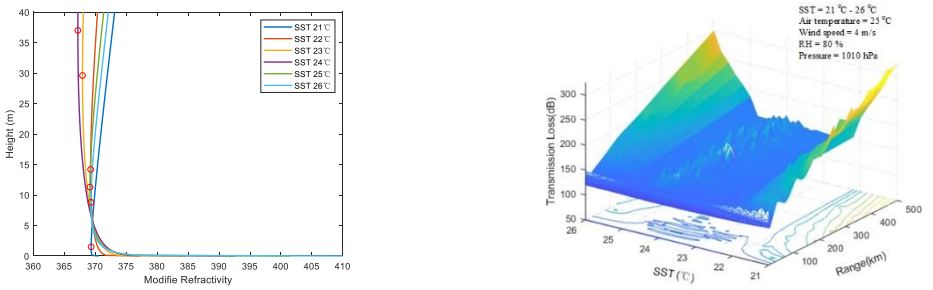


**b)** Transmission loss under different SST

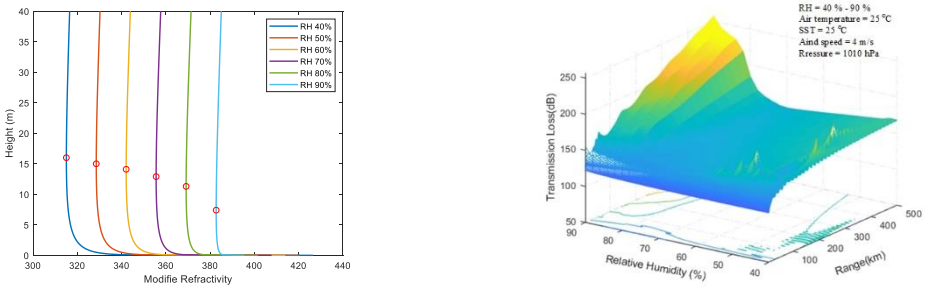


**c)** Transmission loss under different RH

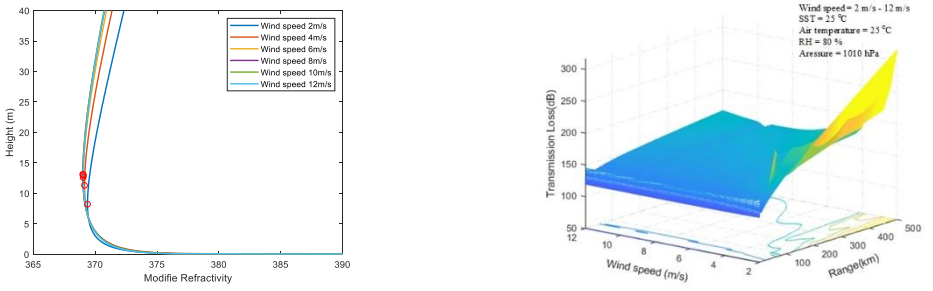


**d)** Transmission loss under different wind speed

**Figure 13.** Modified refractivity profiles and transmission loss at 10GHz with different meteorological parameters.

Modified refractivity profile and transmission loss are mainly affected by ASTD, RH, and wind speed. ASTD determines whether the condition of the evaporation ducts is stable.

In most cases, high sea air temperature differences in near neutral or stable conditions correspond to strong signal strength. It is more conducive to signal transmission when RH decreases and wind speed increases.

### 4.2 Analysis of regional communications in typical time-periods

For the construction of the regional transmission system and the planning of the communication system based on the evaporation duct, it is necessary to master the regional propagation characteristics, understand the transmission loss and range under the current transmission conditions. Distribution characteristics in a large area at the interval of time can be obtained based on the monitoring results of the evaporation ducts, from which the modified refractive index profile can be extracted, and then the path loss at different distances can be calculated.

Considering the complexity of conduct statistics on the propagation characteristics of the past 10 years, this paper selects 1st day of February, May, June, November in 2020 at 8 o'clock as the representative time to analyze EDH, transmission loss, transmission range in the SCS. 300km is taken as the transmission radius to complete the transmission loss calculation. By setting fixed communication stations on the islands in the SCS, communication in most areas can be guaranteed with a communication radius of 300km. The capacity of the communication system is set as the threshold to analyze the maximum transmission range.

The communication system capability $A$ is mainly composed of the transmitting power $P_t$, transmitting antenna gain $G_t$, receiving antenna gain $G_r$, receiver sensitivity $L$, system loss $S$, and system margin $M$, which can be expressed as

$$A = P_t + \mathrm{G}_t + G_r - L - S - M \tag{3}$$

The meanings of each parameter are shown in Table 1. With the values of typical communication equipment, and the communication system capacity $A$ is 190dB.

**Table 1.** Communication system parameters of typical communication equipment.

| Parameters | Symbol | Value |
|---|---|---|
| Transmission power | $P_t$ | 40 dBm/10 W |
| Transmitting antenna gain | $G_t$ | 30 dBi |
| Receiving antenna gain | $G_r$ | 30 dBi |
| Receiver sensitivity | $L$ | -100 dBm |
| System loss | $S$ | 5 dB |
| System margin | $M$ | 5 dB |

Figure 14 shows EDH, transmission loss, transmission range in the SCS. During the statistical period, the transmission loss and communication distance are constantly changing with the vary of meteorological conditions in a month. The overall ocean evaporation duct is relatively stable, and the transmission effect is great in February.

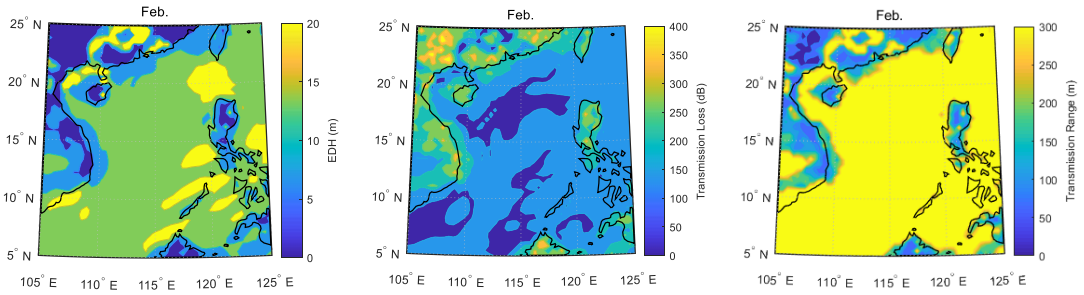


**a)** EDH, transmission loss, transmission range in Feb. 1, 2020 at 8:00

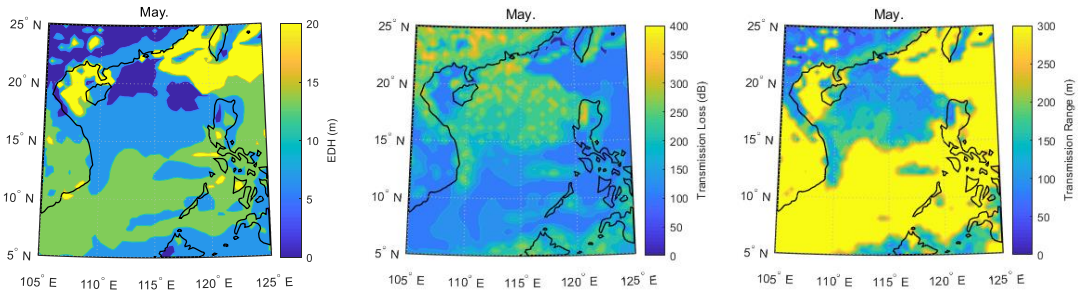


**b)** EDH, transmission loss, transmission range in May. 1, 2020 at 8:00

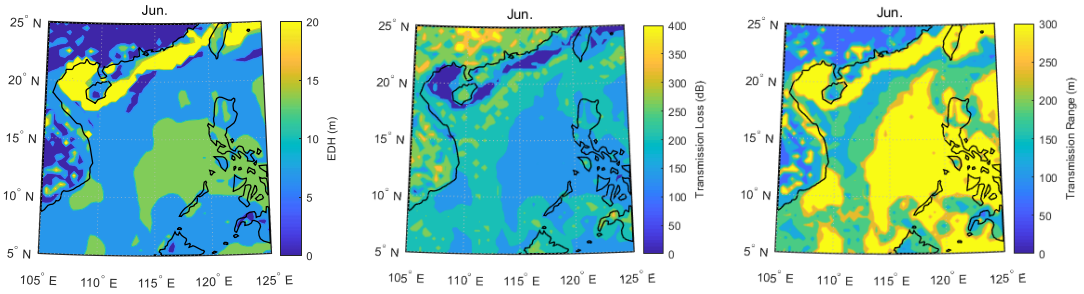


**c)** EDH, transmission loss, transmission range in Jun. 1, 2020 at 8:00

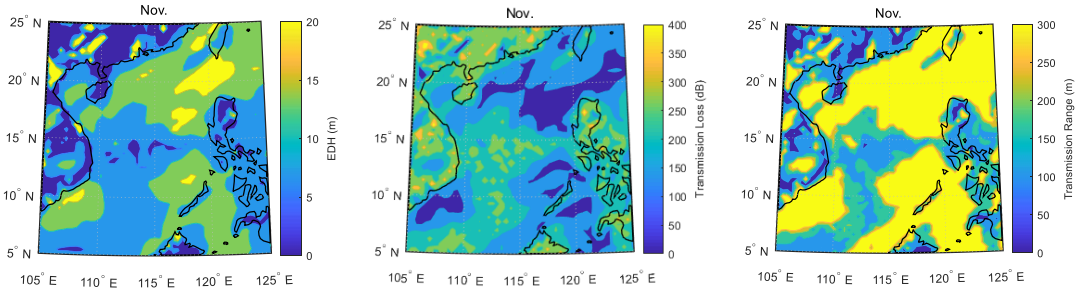


**d)** EDH, transmission loss, transmission range in Nov. 1, 2020 at 8:00

**Figure 14.** Regional propagation characteristics in typical times.

Transmission loss at 300km is concentrated between 150dB and 160dB, and the transmission range at most locations in the ocean can reach 300km. EDH in the northern and western oceans decreased in May and June, which was reflected in the communication effect that the transmission loss in this region was more than 200dB, and the transmission range also decreased to less than 200km. As the height increases gradually in the northern coastal region, an optimal channel appears in terms of transmission loss and range. In November, the

conditions in the northern ocean began to improve, and the transmission effect was also enhanced. Communications in the central areas are still poor.

By analyzing the propagation effect in the SCS, the database of propagation characteristics in the typical time and position domain is constructed, which can provide auxiliary decision-making information for the work of transmission system and an important basis for the design of communication system.

### 4.3 Analysis of communication effect in a typical location

From consideration of section 3, the distribution with EDH and meteorological parameters in the coastal land, inland, and Hainan island areas shows a similar pattern. The insufficient strength of the evaporative duct and the low height in part time may have poor effects on the signal transmission. To further analyze the performance of continuous communication effects by evaporation ducts, we take transmission conditions in 2020 at typical positions of Land-Sea Interface, Taiwan Strait, and Central SCS as the main communication scenarios in the analysis.

In the simulation of the communication effect, we follow the typical communication system parameters in Table 1 for simulation analysis. Transmission loss, signal-to-noise ratio (SNR), and bit error rate (BER) under different modulations are introduced as parameters to evaluate the communication effect for the 300km transmission range. It was assuming that the external electromagnetic environment is broadband and additive white Gaussian noise, the bit-error-rate (BER) characteristics against general modulation modes (such as 2FSK, BPSK, QPSK, MSK, 16-QAM, and 64-QAM) can be obtained by (Wang et al., 2016). According to typical data communication theory, the mapping relation between the grades of transmission performance (can be expressed quantitatively by BER) and SNR corresponding to different modulation modes can be obtained. As shown in Figure 15 and Table 2, it is no effect on the normal operation of the data communication ($BER<10^{-5}$) when the received SNR is better than 13.3dB, 9.9dB, 9.9dB, 9.9dB, 14.0dB, and 18.6dB for modulation modes of 2FSK, BPSK, QPSK, MSK, 16-QAM, and 64-QAM. While it is unable to work normally and communication interrupted ($BER>10^{-1}$) when the received SNR is inferior to 2.2dB, -0.8dB, -0.8dB, -0.8dB, 6.2dB, and 11dB for the above six modulation modes.

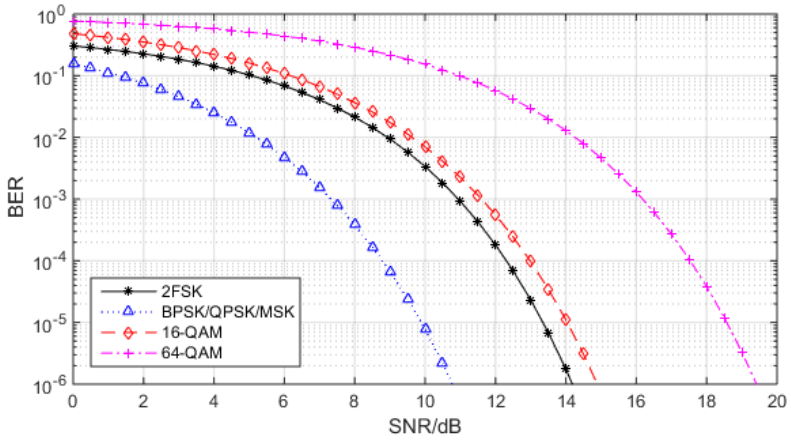


**Figure 15.** The level of different communication performance corresponding to BER and SNR.

**Table 2.** The level of different communication performance corresponding to BER and SNR.

| Grade of communication performance | | SNR corresponding to different modulation modes (dB) | | | |
|---|---|---|---|---|---|
| **Communication performance** | **BER (dB)** | **2FSK** | **BPSK/ QPSK/MSK** | **16-QAM** | **64-QAM** |
| No effect on the normal operation of the communication system | $<10^{-5}$ | >12.6 | >9.6 | >14.0 | >18.6 |
| Message communication can be realized but the quality of packet communication is poor | $[10^{-5}, 10^{-3})$ | [9.8, 12.6) | [6.8, 9.6) | [11.6, 14.0) | [16.2, 18.6) |
| Message communication is barely realized and packet communication is not possible | $[10^{-3}, 10^{-2})$ | [7.3, 9.8) | [4.3, 6.8) | [9.6, 11.6) | [14.2, 16.2) |
| Message and packet communication systems cannot be implemented | $[10^{-2}, 10^{-1})$ | [2.2, 7.3) | [-0.8, 4.3) | [6.2, 9.6) | [11.0, 14.2) |
| Unable to work normally and communication interrupted | $\geq 10^{-1}$ | ≤2.2 | ≤-0.8 | ≤6.2 | ≤11.0 |

4.3.1 Land-Sea Interface

The land-sea interface area shows obvious seasonal characteristics, and the transmission loss is lower in spring and winter, while large losses occurred in summer frequently. Solar radiation energy is higher in summer, and the land absorbs the solar radiation energy faster causes the ground to warm up. The solar radiation energy is absorbed and stored in the seawater, which makes sea-land breeze circulation easily appear in coastal areas, affecting the duct characteristics and the transmission effect (Plant et al., 2002).

In Figure 16, monthly statistical results were analyzed under the Land-Sea Interface scenario for the 300 km transmission range in 2020. The overall regional communication effect is lacking, and the available signal probability is 53.93%. The green line in the figure is the communication system capability *A*, which is also the threshold for the received signal. For the land-sea Interface, a statistical box with lower quartile, median, and upper quartile in October and November are preferable, which can meet the requirements of the transmission system. To quantitatively analyze the Continuous transmission performance under the Land-Sea Interface scenario, Figure 17 depicted the received SNR and BER with BPSK, QPSK, and MSK modulation. The green line represents the condition with no effect on the normal operation of the communication system, while the red line is unable to work normally, and communication is interrupted. It shows that the BER can be superior to $10^{-5}$ with BPSK, QPSK, and MSK modulation modes for 73.57% of the time, the ratio with $10^{-1}$ is 77.94%. In late October and mid-November, large periods of unavailability occurred with high BER. According to the hourly statistical results of these two months in Figure 18, the corresponding transmission parameters at each time are relatively balanced. It has also been verified that hourly communication in the land-sea interface area is less sensitive to the alternation of day and night.

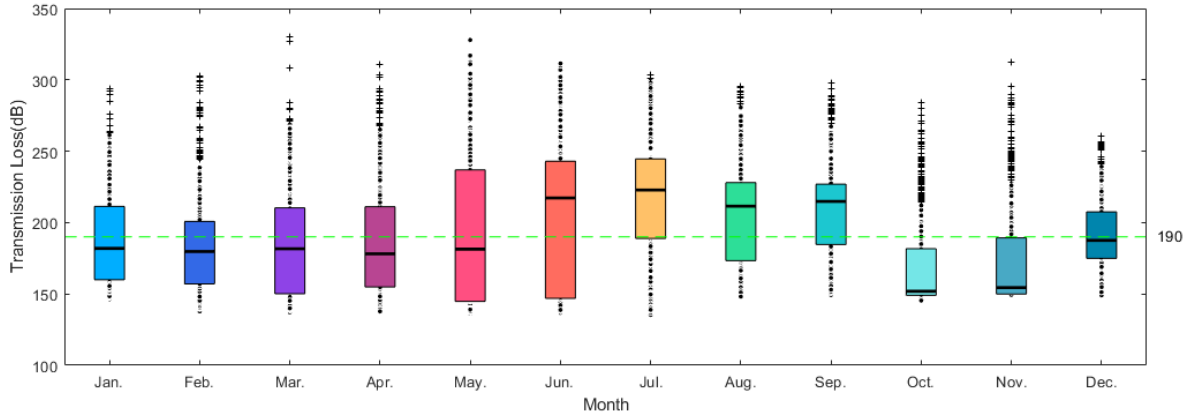


565

566 **Figure 16.** Monthly statistical results for the 300km transmission range in the land-sea interface area
567 during 2020.

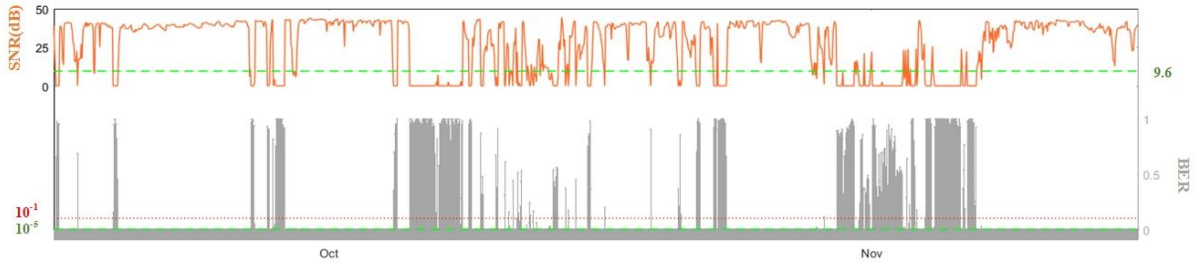


568

569 **Figure 17.** Continuous communication effect analysis in the land-sea interface area.

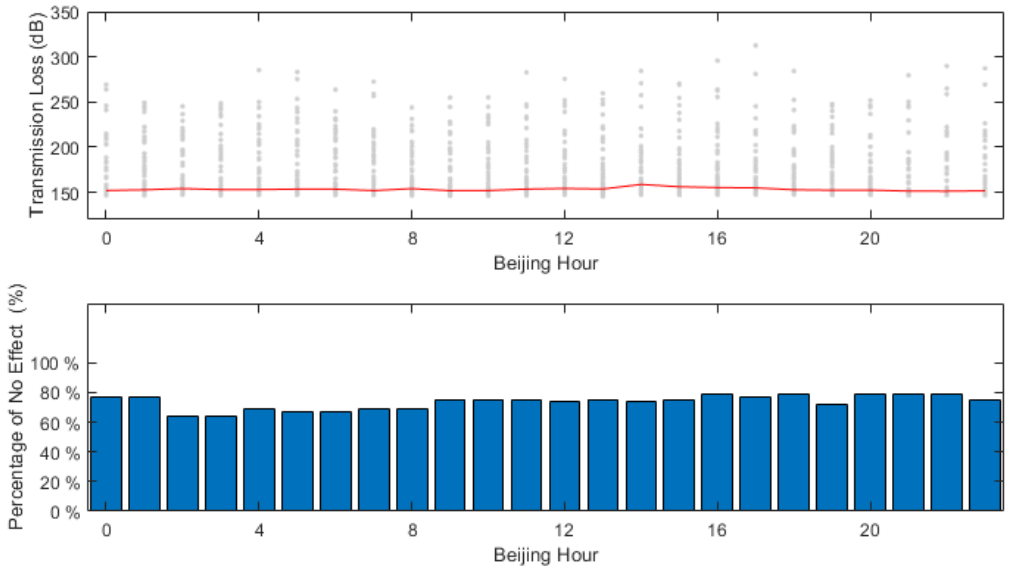


570

571 **Figure 18.** Hourly statistical results under Land-Sea Interface area in October and November.

572 In the land-sea interface area, continuous communication can be realized in spite of
573 diurnal variation. Overall, the available probability may not be high due to the great influence
574 of meteorological conditions.

### 4.3.2 Taiwan Strait

The diurnal regularity of the Taiwan Strait is obvious due to the change of meteorological parameters of the Kuroshio Current (Feng et al., 2015) and land-sea boundary. The transmission effect under this scenario for the 300 km transmission range is shown in Figure 19, and the parameters such as available probability and transmission loss with 9 m transmitting height and 8m receiving height were analyzed from the hour and day time dimensions.

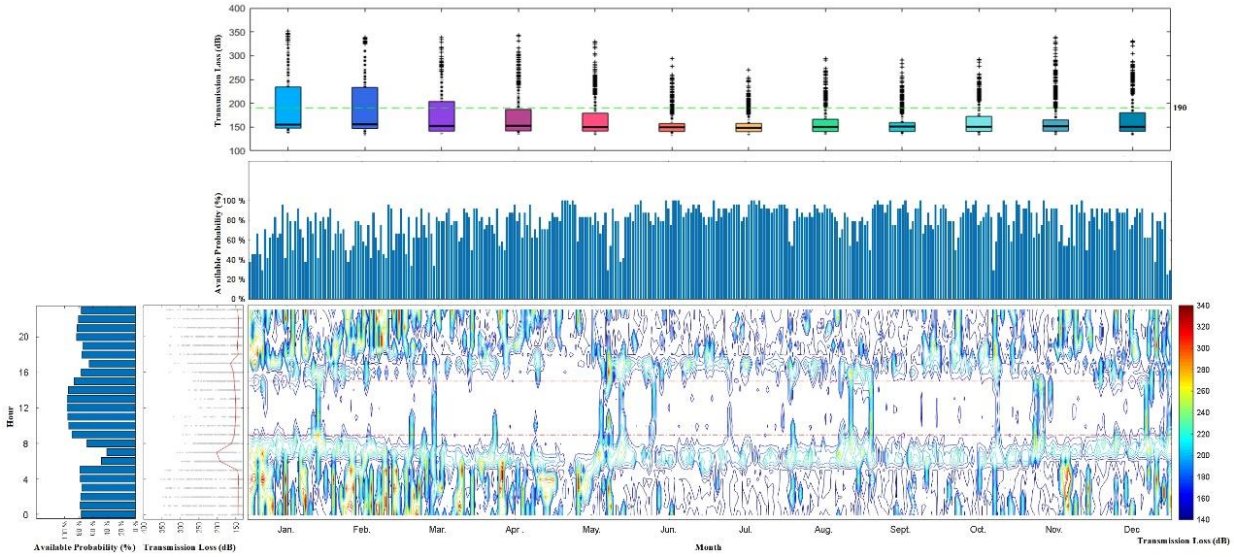


**Figure 19.** Communication effect under Taiwan Strait area for 300km transmission range in 2020.

Transmission loss in Taiwan Strait is significantly lower than that in the other two locations. There are few points of high loss represented by yellow, and most of the time is dark blue with low loss. The available annual probability reached 78.79%. A superior "channel" from 9:00 to 14:00 is represented in Figure 19. The signal transmission effect is stable and passable, which may supply effective guarantees for wireless communication. The available signal probability is the highest from 12:00 to 13:00, reaching 96.72%. Median transmission loss is 150.1dB, which exceeds 37.82dB with the communication system capacity *A* is 190 dB and provides extremely favorable conditions for signals transmission. Transmission loss is large at sunrise period (from 5:00 to 9:00) and sunset period (from 15:00 to 18:00) throughout the year because of a consequence serious signal interrupts impact on the communication. The maximum median loss is 202.41dB at 7:00, and the available probability is 40.44%. As can be seen from statistical results, the monthly mid-values vary little. The transmission effect is poor from January to April, and the degree of dispersion between signals is high. It is easy to cause signal interruption while transmission loss of multiple periods exceeds 190dB. Otherwise, the transmission effect in summer and autumn is significantly improved, and the available signal probability in June and July exceeds 75% continuously, indicating a good accessibility effect can be got.

Since the SNR is high at 12:00, a high modulation mode can be considered to achieve a high symbol transmission rate. Therefore, we tried to analyze the BERs with different modulation modes in Table 2. In Figure 20, transmission performance is well during most of the days at noon. The time percentage statistics of no effect on the normal operation of the transmission system (defined as “high-quality transmission”) exceed 95% by BPSK, QPSK, MSK and QAM modulation. Data transmission performance is optimum by BPSK, QPSK, and MSK modulation, which can reach 95.9% with high-quality transmission performance.

The percentage of 64-QAM is only 0.27% lower than that of other modulation modes, and it can be chosen to guarantee the symbol transmission rate while adequate SNR can be provided.

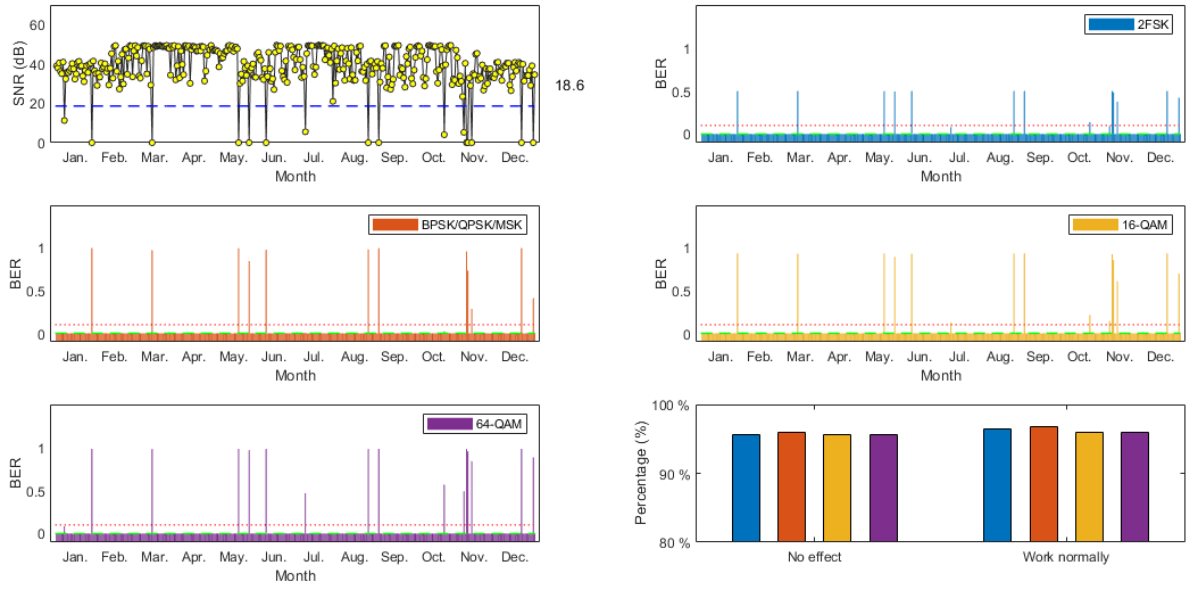


**Figure 20.** The SNR and BER in the Taiwan Strait area in 12:00.

As Figure 21, the high-quality time percentage of six modulations is up to 90% at noontime from 9:00 to 14:00, and it can also maintain more than 70% in nighttime from 19:00 to 4:00. Sunrise Time and Sunset Time are the worst-performing periods, and the high-quality time percentage of six modulations is only about 50% from 5:00 to 8:00 and 65% from 15:00 to 18:00 separately. Due to the sunrise time's strong fading of transmission signals, the high-quality time percentages of BPSK, QPSK, and MSK modulations are significantly different. These values are 48.22%, 52.32%, 52.32%,52.32%, 48.16%, and 47.68%, separately. The percentage in other periods showed little difference with modulations changed, which is also consistent with the qualitative analysis from Figure 20.

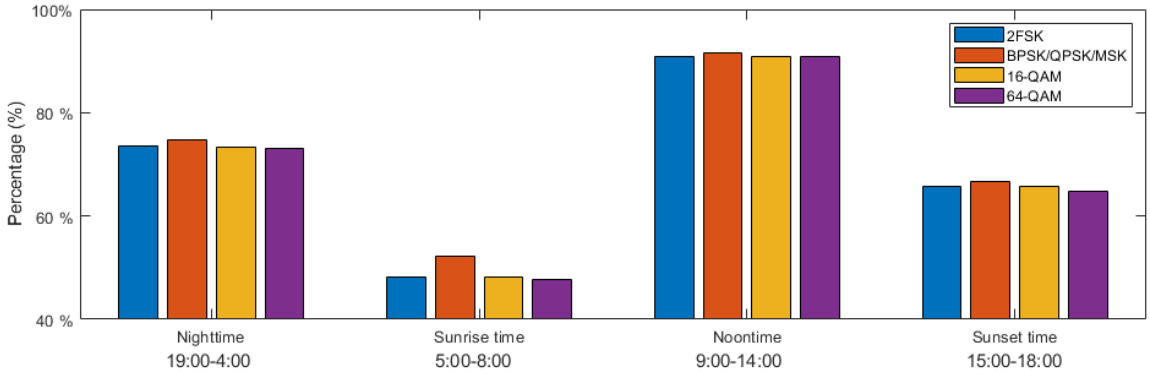


**Figure 21.** The time percentage statistics of no effect on the normal operation of the transmission system with 2FSK, BPSK, QPSK, MSK, 16-QAM, and 64-QAM modulation in the Taiwan Strait area.

### 4.3.3 Central SCS

Similar to the Land-Sea Interface, the monthly statistical results of the Central SCS also show significant seasonal characteristics in Figure 22. The difference is that the optimum communication condition shows in spring. 190dB is taken as the transmission link

accessibility to conduct statistics results in Central SCS, and more than 75% of data between January and April were below that level. The transmission effect in Central SCS is more stable, which shows the characteristics of the open sea. The continuous accessibility is strong in spring, and the communication effect is more balanced in other months. The annual signal available probability is 64.87%.

Considering that transmission loss became significantly larger after May, analysis results from January to April are shown in Figure 23, which illustrates the signal transmission effect. Unlike Taiwan Strait, the communication in this scenario does not show significant circadian regularity. The overall transmission effect is more balanced, which can realize continuous signal transmit in a long period. However, the transmission effect is greatly affected by meteorological parameters, and there may be a continuous period of communication failure when the conditions are poor. In Figure 24, SNR and BER with BPSK, QPSK, and MSK modulation in continuous communication was analyzed under the Central SCS area. It shows that the BER can be superior to $10^{-5}$ with BPSK, QPSK, and MSK modulation modes for 80.72 % of the time, the ratio with $10^{-1}$ is 85.57 %. The longest continuous connection time is over 163 hours, which provides favorable conditions for signal transmission.

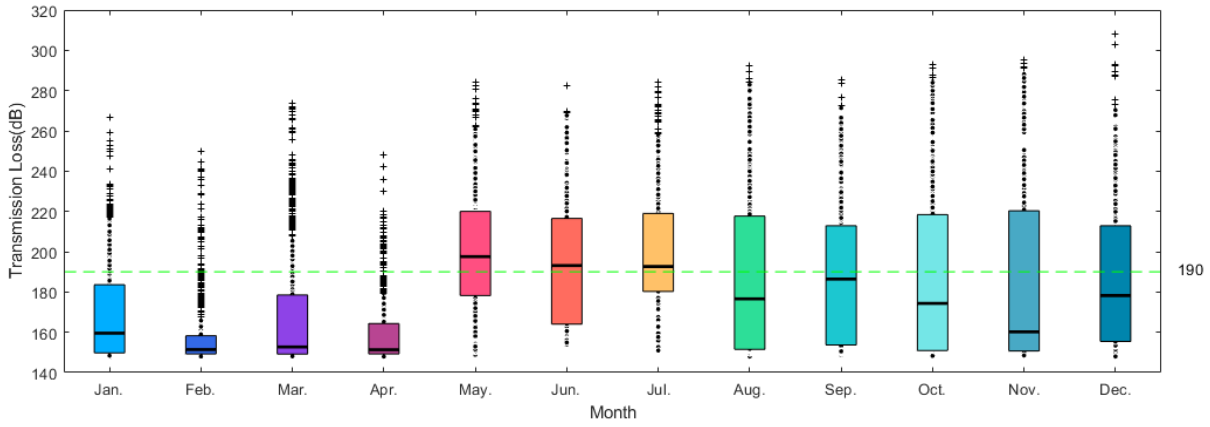


**Figure 22.** Monthly statistical results under Land-Sea Interface area for 300km transmission range in 2020.

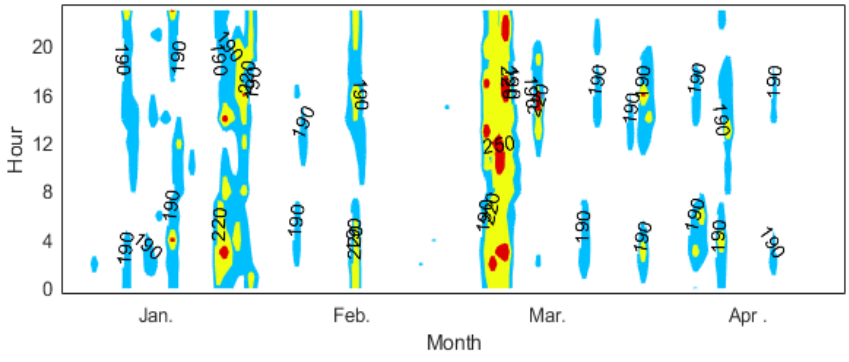


**Figure 23.** Statistical communication effect under Central SCS area.

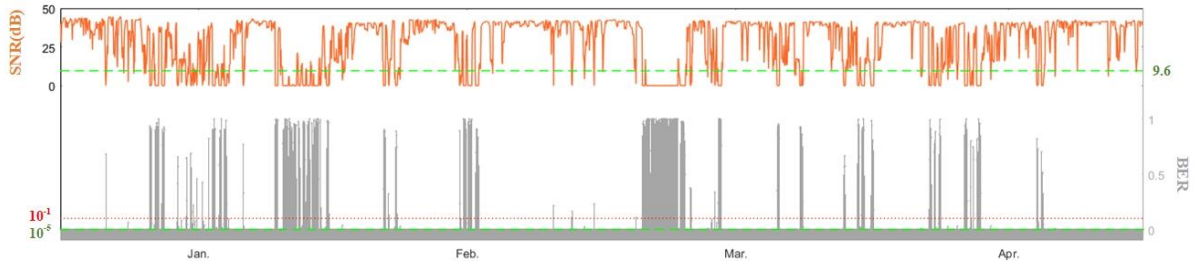


**Figure 24.** Continuous communication effect analyzation under Central SCS area.

## 5. Conclusions

In this paper, high resolution spatial-temporal statistical database of the evaporation duct over the SCS was formed by using the statistical analyzed method, and the characteristics at typical locations have also been analyzed. Meteorological factors such as RH, wind speed, and ASTD are the main factors that impact the evaporation duct. The EDH was the highest at 18:00 and the lowest at 6:00-8:00 before sunrise. The coastal channel has a width of more than 300km appeared in the northern coastal area from May to July, which offers optimum conditions for transmission. Affected by the sea-land breeze and the Kuroshio warm current, Taiwan Strait has the highest statistical EDH for 18.37m in the SCS. The height of Central SCS is maintained between 10m - 12m, and the average height is 11.20 m.

Transmission loss has the characteristics of "pipe adaptation" under meteorological parameters. Regional communication effect analysis shows that: transmission range of 300km can be achieved under typical communication parameters base on evaporation ducts in February. The transmission in Land-Sea Interface and Central SCS area show significant seasonal characteristics and can achieve continuous communication for a long time. The percentage of high-quality transmission time is 80.72 % with BPSK, QPSK, and MSK modulation in the Central SCS area, and the longest continuous connection time is over 163 hours. Transmission in Taiwan Strait presents diurnal regularity. A superior "channel" emerges at a fixed period from 9:00 to 14:00, which may supply stable and passable conditions for wireless communication. The high-quality time percentage of 64-QAM modulations is 95.63% at noontime from 9:00 to 14:00.

Analysis of propagation has important implications for evaporation duct communication system design and provides auxiliary decision information for normal system operating. Furthermore, we will combine the data from fixed meteorological stations to systematically comb the spatial-temporal distribution characteristics of the evaporation duct, and propagation characteristics experiments will also be carried out to cross-validate the simulation propagation results.

## Acknowledgments

The meteorological parameters datasets used in this work can be downloaded from the NCEP Climate Forecast System website (https://rda.ucar.edu/datasets/ds094.1/#!access). This work was supported in part by National Natural Science Foundation of China (No. 62031008), and Qingdao National Laboratory for Marine Science and Technology of China under Grant QNLM2016ORP0411.

## References


Alappattu D. P., Wang Q. and Kalogiros J. (2016), Anomalous propagation conditions over eastern Pacific Ocean derived from MAGIC data. *Radio Science*, 51(7), 1142-1156. https://doi.org/ 10.1002/2016RS005994.

Barrios A. E., Anderson K. and Lindem G. (2006), Low Altitude Propagation Effects - A Validation Study of the Advanced Propagation Model (APM) for Mobile Radio Applications. *IEEE Transactions on Antennas and Propagation*, 54(10), 2869-2877. https://doi.org/ 10.1109/TAP.2006.882163.

Babin S M, and Dockery G D. (2002), LKB-Based Evaporation Duct Model Comparison with Buoy Data. *Journal of Applied Meteorology and Climatology*, 41(4), 434-446.

Babin S M, Young G S, and Carton J A. (1997), A new model of the oceanic evaporation duct. *Journal of Applied Meteorology and Climatology*, 36(3), 193-204.

Bean B. R., and Dutton E. J. (1966), *Radio Meteorology*. Technical report archive & image library.

Battan L. J. (1973), *Radar Observation of the Atmosphere*. University of Chicago Press.

Barrios A E, and Patterson W L. (2002), *Advanced Propagation Model (APM) Ver. 1.3.1 Computer Software Configuration Item (CSCI) Documents*.

Booker H, and Walkinshaw W. (1946), The mode theory of tropospheric refraction and its relation to wave-guides and diffraction. *Meteorological factors in radio-wave propagation*, 80-127

Burk S D, Haack T, Rogers L T, and Wagner L. J. (2003), Island Wake Dynamics and Wake Influence on the Evaporation Duct and Radar Propagation. *Journal of Applied Meteorology and Climatology*, 42(3), 349-367. https://doi.org/ 10.1175/1520-0450(2003)0422.0.CO;2.

Cheng Y., Zhou S., Wang D., Lu Y., Huang K., Yao. J., and You X. (2016), Observed characteristics of atmospheric ducts over the South China Sea in autumn, *Chinese Journal of Oceanology and Limnology*, 34(3), 619-628. https://doi.org/10.1007/s00343-016-4275-2.

Choi J. (1997), *Performance Comparison of Tropospheric Propagation Models: Ray-Trace Analysis Results Using Worldwide Tropospheric Databases*. DTIC Document.

Fairall C. W., Bradley E. F., Hare J. E., Grachev A. A., and Edson J. B. (2003), Bulk parameterization of air-sea fluxes: Updates and verification for the COARE algorithm. *Journal of Climate*, 16(4), 571-591. https://doi.org/ 10.1175/1520-0442(2003)016<0571:BPOASF>2.0.CO;2.

Feng N., Xue H., and Fei Y. (2015), Kuroshio intrusion into the South China Sea: A review. *Progress in Oceanography*, 137, 314-333. https://doi.org/ 10.1016/S1001-6058(07)60010-9.

Frederickson P. A., Davidson K. L., and Goroch A. K. (2000), Operational bulk evaporation duct model for MORIAH version 1.2. *Naval Postgraduate School, Monterey*, CA, USA, Tech. Rep..

Gary W. C. (1990), *Assessment of atmospheric effects on VHF and UHF Communications*. California: Naval Postgraduate School.

Grachev A. A., and Fairall C. W. (1997), Dependence of the Monin–Obukhov Stability Parameter on the Bulk Richardson Number over the Ocean. *Journal of Applied Meteorology and Climatology*, 36(4), 406-415. https://doi.org/ 10.1175/1520-0450(1997)036<0406:DOTMOS>2.0.CO;2.

Grachev A. A., Andreas E. L., Fairall C. W., Guest P. S., and Persson P. O. G. (2007), SHEBA flux–profile relationships in the stable atmospheric boundary layer. *Boundary-Layer Meteorology*, 124(3), 315-333. https://doi.org/ 10.1007/s10546-007-9177-6.

Haack T., and Burk S. D. (2001), Summertime Marine Refractivity Conditions along Coastal California. *Journal of Applied Meteorology and Climatology*, 40(4), 673-688.

Hao X., Guo L., Lin L., Li Q. and Zhang Y. (2016), The statistic and analysis of atmospheric ducts worldwide using radiosonde data. *2016 11th International Symposium on Antennas, Propagation and EM Theory (ISAPE)*, 911-914. https://doi.org/10.1109/ ISAPE.2016.7834111.

Hardin R. H., and Tappert FD (1973), Applications of the Split-Step Fourier Method to the Numerical Solution of Nonlinear and Variable Coefficient Wave Equations. *Siam Review*, 15(1), 423.

Jiang Q., Wang Q., Wang S., Gaberek S. (2020), Turbulence adjustment and scaling in an offshore convective internal boundary layer: a CASPER case study. *Journal of the Atmospheric Sciences*, 77(5). https://doi.org/ 10.1175/JAS-D-19-0189.1.

Karimian A., Yardim C., Gerstoft P., W. S. Hodgkiss and Barrios A. E. (2012), Multiple Grazing Angle Sea Clutter Modeling. *IEEE Transactions on Antennas and Propagation*, 60(9), 4408-4417. https://doi.org/ 10.1109/TAP.2012.2207033.

Ko H W, Sari J W, and Skura J P. (1983), Anomalous microwave propagation through atmospheric ducts. *Johns Hopkins APL Technical Digest*, 4, 12-26.

Lin F J, Liu C G, Cheng S, and Yang Y P. (2005), Statistical analysis of marine atmospheric duct. *Chinese Journal of Radio Science*, 20(1), 64-68. https://doi.org/10.3969/j.issn.1005-0388.2005.01.014.

Liu C., Pan Z., and Li G. (1996), Statistical analysis of occurrence and characteristics of atmospheric ducts in China. *Chinese Journal of Radio Science*, 11(2), 60-66.

Liu W. T., Katsaros K. B., and Businger J. A. (1979), Bulk Parameterization of Air-Sea Exchanges of Heat and Water Vapor Including the Molecular Constraints at the Interface. *Journal of the Atmospheric Sciences*, 36(9), 1722-1735. https://doi.org/ 10.1175/1520-0469(1979)036<1722:BPOASE>2.0.CO;2.

Mcallister M., Booker L., Fowler D. K., and Haran T. M. (2014), MODIS Data and Services at the National Snow and Ice Data Center (NSIDC). *AGU Fall Meeting Abstracts*.

Musson-Genon L., Gauthier S., and Bruth E. (1992), A simple method to determine evaporation duct height in the sea surface boundary layer. *Radio Science*, 27(5), 635-644. https://doi.org/ 10.1029/92RS00926.

Newton D. A. (2003), *COAMPS Modeled Surface Layer Refractivity in the Roughness and Evaporation Duct Experiment 2001*. California: Naval Postgraduate School.

Paulus R. A. (1985), Practical application of an evaporation duct model. *Radio science*, 20(4), 887-896. https://doi.org/10.1029/RS020i004p00887.

Plant R. S., and Atkinson B. W. (2002), Sea-Breeze Modification of The Growth of a Marine Internal Boundary Layer. *Boundary-Layer Meteorology*, 104(2), 201-228. https://doi.org/ 10.1023/A:1016045229957.

Saha S. (2012), *NCEP Climate Forecast System Version 2 (CFSv2) Monthly Products*. Research Data Archive at the National Center for Atmospheric Research, Computational and Information Systems Laboratory. https://doi.org/10.5065/D69021ZF.

Shi Y., Zhang Q., Wang S., Yang K., and Ma Y. (2019), Impact of Typhoon on Evaporation Duct in the Northwest Pacific Ocean. *IEEE Access*, 99. https://doi.org/ 10.1109/ACCESS.2019.2932969.

Stull R. B. (1988), *An Introduction to Boundary Layer Meteorology*. Springer Netherlands.

Surhone L. M., Tennoe M. T., and Henssonow S. F. (2011), National Data Buoy Center. *Betascript Publishing*.

Ulate M., Wang Q., Haack T., Holt T., Alappattu D. P. (2018), Mean offshore refractive conditions during casper-east field campaign. *Journal of Applied Meteorology and Climatology*, 58(4). https://doi.org/ 10.1175/JAMC-D-18-0029.1.

Wang J., Zhang J., Wang R., and Li X. (2016), Relativity of Electromagnetic Environment and Down-to-earth Complexity Evaluation. *Journal of Electronics & Information Technology*, 38(5), 1249-1255. https://doi.org/ 10.11999/JEIT150947.

Wang J., Yang C., and Yan N. N. (2021), Study on digital twin channel for the B5G and6G communication. *Chinese journal of radio science*, 36(3), 340-348.

Woods G. S., Ruxton A., Huddlestone-Holmes C. and Gigan G. (2009), High-Capacity, Long-Range, Over Ocean Microwave Link Using the Evaporation Duct. *IEEE Journal of Oceanic Engineering*, 34(3), 323-330. https://doi.org/ 10.1109/JOE.2009.2020851.

Yang K., Ma Y., and Shi Y. (2009), Spatio-temporal distributions of evaporation duct for the West Pacific Ocean. *Acta Physica Sinica*, 58(10), 7339-7350. https://doi.org/ 10.1360/972009-782.

Yang K, Zhang Q, Shi Y. (2017), Interannual variability of the evaporation duct over the South China Sea and its relations with regional evaporation. *Journal of Geophysical Research: Oceans*. https://doi.org/10.1002/2017JC012683.

Yardim C., Gerstoft P., Hodgkiss W. S. and Rogers T. (2007), Statistical Estimation of Refractivity from Radar Sea Clutter. *2007 IEEE Radar Conference*, 938-943. https://doi.org/ 10.1109/RADAR.2007.374345.

Zhao W.; Zhao J.; Li J.; Zhao D.; Huang L.; Zhu J.; Lu J.; Wang X. (2021), An evaporation duct height prediction model based on a Long Short-Term Memory Neural Network. *IEEE Transactions on Antennas and Propagation*. https://doi.org/10.1109/TAP.2021. 3076478.

Zhao X. F., and Huang S. (2012), Estimation of Atmospheric Duct Structure Using Radar Sea Clutter. *Journal of the Atmospheric Sciences*, 69(9), 2808-2818. https://doi.org/10.1175/ JAS-D-12-073.1.

Zhao X. F., Wang D. X., Huang S. X., Huang K., and Chen J. (2013), Statistical estimations of atmospheric duct over the South China Sea and the Tropical Eastern Indian Ocean. *Chinese Science Bulletin*, 58(23), 2794-2797. https://doi.org/10.1007/s11434-013-5942-8.

Zhu X., Li J., Zhu M., Jiang Z., Li Y. (2018), An Evaporation Duct Height Prediction Method Based on Deep Learning. *IEEE Geoscience and Remote Sensing Letters*, 15(9), 1307-1311. https://doi.org/10.1109/LGRS.2018.2842235.

Zuo H., Balmaseda M. A., Tietsche S., Mogensen K., and Mayer, M. (2019), The ECMWF operational ensemble reanalysis–analysis system for ocean and sea ice: a description of the system and assessment. *Ocean Science*, 15, 779–808. https://doi.org/ 10.5194/os-15-779-2019.